nature nanotechnology

Article

https://doi.org/10.1038/s41565-026-02270-6

Atomic-scale visualization of three-dimensional magnetization vectors with competing spin Hamiltonian interactions

Received: 24 January 2026

Accepted: 4 August 2026

Published online: 8 October 2026

Check for updates

Qi Wang[1,2,3,9], Miao Zhang[1,2,3,9], Gustav Bihlmayer[4], Jizhou Li[5], Anhua Wu[6], Wenhao Di[6], Liangbi Su[6], Yulei Song[1,2,3], Shih-Wei Hung[1], Jan Rusz[7], Rafal E. Dunin-Borkowski[8] & Xiaoyan Zhong[1,2,3]

The spin Hamiltonian describes the energy of a magnetic system, which originates from interactions between electron spins that have a three-dimensional (3D) vectorial nature and atomic-scale arrangement. It is crucial to know the energy contributions associated with spin behaviour, such as superexchange coupling, Dzyaloshinskii–Moriya interaction, Zeeman energy in external fields and single-ion anisotropy (SIA), for a fundamental understanding of the ground state and dynamics of magnetic materials. An experimental method, capable of resolving local 3D spin vectors on the atomic scale, is needed to provide direct correlation between the competing energy terms and corresponding atomic configurations. Here we demonstrate a beam-shift-based four-dimensional electron magnetic circular dichroism technique, which achieves quantitative 3D vector magnetometry and infers the energy contributions to the spin Hamiltonian on an individual atomic plane basis. The spatial resolution of 2.25 Å enables evaluation of spin Hamiltonian energy terms within individual atomic planes. In a canted antiferromagnet, $YFeO_3$, we confirm an asymmetric spin reorientation of the magnetic spin moments on the two antiferromagnetic spin sublattices. The inferred superexchange coupling, Dzyaloshinskii–Moriya interaction, SIA and Zeeman energies provide atomic-level insight into the interplay between these spin interactions during a field-induced spin reorientation transition. The observed asymmetry in spin reorientation angle arises primarily from the SIA and opposite Zeeman energies of the adjacent antiferromagnetically coupled atomic planes, resulting in both magnetic spin moments being nearly aligned with the external magnetic field. By bridging the gap in imaging resolution for 3D spin vectors and atomic positions, our method opens an avenue for the atomic-scale characterization and engineering of the energetics described by the spin Hamiltonian.

A full list of affiliations appears at the end of the paper. e-mail: xzhong25@cityu.edu.hk

The spin Hamiltonian of a magnetic material is governed by four competing terms[1]: Heisenberg superexchange, Dzyaloshinskii–Moriya interaction (DMI), Zeeman coupling and single-ion anisotropy (SIA)[2–4]. Together, these interactions determine collinear order, spin canting, field-driven alignment and crystallographic spin preferences. Because their magnitudes depend sensitively on bond geometry, atomic displacements and coordination, subtle structural variations can reorganize the magnetic ground state. Their interplay underpins topological skyrmions and hopfions[5,6], helical spin spirals[7], magnetoelectric coupling[8] and weak ferromagnetism[9]. Direct evaluation of the spin Hamiltonian at the atomic scale, however, requires simultaneous knowledge of the local atomic structure and the three-dimensional (3D) spin vectors $\mathbf{S}_i$ of neighbouring sites[10]. This capability remains unavailable: established approaches generally infer spatially averaged Hamiltonian parameters from bulk specimens, nanoscale magnetic domains or domain walls[11,12]. Resolving neighbouring 3D spins together with their atomic environments is therefore essential for determining how local structure governs competing magnetic interactions.

High-spatial-resolution imaging probes two related but distinct vector fields: magnetic induction **B** and magnetization **M**. Transmission electron microscopy (TEM) imaging techniques, including off-axis electron holography[13,14], Lorentz TEM[15,16], electron ptychography[17,18] and differential phase-contrast scanning transmission electron microscopy (STEM)[19,20], visualize the in-plane components of projected **B**. However, in antiferromagnets, these measurements have not resolved magnetic information from individual atomic planes or columns without signal averaging. With tilt-series tomography, electron holography[14] and Lorentz TEM[15,16] can reconstruct all three components of **B** with sub-10-nm resolution, still far from the atomic scale[14]. Instead, electron magnetic circular dichroism (EMCD)[21–23] probes **M** and has resolved the out-of-plane component M_z at atomic-plane resolution[24,25], but has not simultaneously mapped M_x, M_y and M_z at that scale. Atomic-resolution determination of 3D **M** therefore remains unavailable[26], limiting direct analysis of local spin Hamiltonian energetics and their response to structural or external perturbations.

In this study, we report a beam-shift-based 4D EMCD technique that enables quantitative measurement of 3D magnetization vectors on an individual atomic plane basis from a single dataset acquired at one fixed specimen orientation, without a tilt series. We examine the prototype canted antiferromagnetic (AFM) orthoferrite $YFeO_3$ and successfully map its 3D spin vectors atomic plane-by-plane with its magnetic orbital moments nearly quenched[27], thereby revealing DMI-induced spin canting and visualizing the field-induced spin reorientation (SR) transition between Γ_4 and Γ_2 in the presence of a 2.5-T magnetic field[28]. By combining adjacent-plane spin vectors $\mathbf{S}_i$ with their crystallographic atomic positions and spin Hamiltonian constants reported for bulk single crystals, we infer the atomic-plane-resolved superexchange, DMI, SIA and Zeeman energy contributions. The asymmetric rotation of the 3D spin vectors on the two AFM spin lattices to an external magnetic field is observed experimentally and interpreted using the inferred competition between the four spin Hamiltonian energies.

Component-selective 4D EMCD at atomic-plane resolution

Figure 1a outlines the beam-shift 4D EMCD acquisition technique used to obtain component-selective magnetic signals from antiferromagnetically coupled iron atomic planes. $YFeO_3$ is oriented under a three-beam condition (3BC) that excites the selected systematic reflection **G** and places the corresponding AFM-coupled planes parallel to the incident electron beam. An atomic-plane-resolved real-space annular dark-field (ADF) STEM image then defines the beam shift Δx relative to each atomic plane. Critically, the diffraction geometry is adjusted so that the diffraction spot **G** lies along the detector's horizontal axis (Fig. 1c), whereas the energy-dispersive acquisition records momentum transfer q_y and energy loss E (Fig. 1d). The focused probe is rastered across the specimen in the real-space x and y directions while a q_y–E spectrum image is recorded at every probe position; x is perpendicular and y is parallel to the AFM planes. The resulting 4D dataset, x–y–q_y–E, links atomic-plane position, transverse momentum transfer and energy loss within a single fixed-orientation acquisition.

We have also developed the theory of atomic-scale EMCD imaging of 3D magnetization vectors, for which detailed information is available in the Methods. The magnetic part of the double-differential cross-section (DDCS), which contains contributions from all of the $M_x(E)$, $M_y(E)$ and $M_z(E)$ components, can be expressed as

$$\frac{\partial^2\sigma}{\partial E\partial\Omega}\Big|_{\mathrm{Mag}} \propto \sum_{\mathbf{k},\mathbf{G}} \frac{1}{q^2 q'^2} \begin{vmatrix} G_x & q_x & 2|T_{\mathbf{G}}|M_x(E) \\ G_y & q_y & \sin\frac{2\pi\Delta x}{d} M_y(E) \\ G_z & q_z & \sin\frac{2\pi\Delta x}{d} M_z(E) \end{vmatrix} = \sum_{\mathbf{k},\mathbf{G}} S(\Delta x, \mathbf{q}, \mathbf{G}, \mathbf{M}(E)), \quad (1)$$

Here, Δx denotes the lateral probe displacement relative to an antiferromagnetically coupled atomic plane of spacing d, q_y is the measured transverse momentum transfer and **G** labels a reciprocal-lattice vector; full definitions of the remaining quantities are provided in Supplementary Information, section 1.1. For detection of the $M_y(E)$ and $M_z(E)$ components, the Fourier shift theorem converts beam shift Δx into a phase modulation of the reciprocal-space probe wavefunction, producing the $\sin\frac{2\pi\Delta x}{d}$ dependence in equation (1). Sensitivity to $M_x(E)$ arises from interference between the incident probe and Bragg-scattered beams. Consequently, the coefficients multiplying the three components exhibit distinct even or odd symmetries under reversal of Δx, q_y, or both (Fig. 1e–g). Because Δx is controlled in real space and q_y is measured in momentum space, these symmetries can be isolated from a single 4D EMCD dataset. We therefore define three analysis strategies: $A_z = [S(\Delta x, q_y) + S(-\Delta x, -q_y)] - [S(\Delta x, -q_y) + S(-\Delta x, q_y)]$, $A_y = [S(\Delta x, q_y) + S(\Delta x, -q_y)] - [S(-\Delta x, -q_y) + S(-\Delta x, q_y)]$ and $A_x = [S(\Delta x, q_y) + S(-\Delta x, q_y)] - [S(\Delta x, -q_y) + S(-\Delta x, -q_y)]$. EMCD spectra extracted from one 4D EMCD dataset using the three analysis strategies A_z, A_y and A_x are found to be primarily proportional to $q_y \sin\frac{2\pi\Delta x}{d} M_z(E)$, $-\sin\frac{2\pi\Delta x}{d} M_y(E)$ and $-q_y M_x(E)$, respectively, while contributions from the other two orthogonal directions are substantially minimized. Exact four-point combinations, sign conventions and cross-talk analyses are provided in Supplementary Information, section 1.1 and equations (16), (18) and (20).

The canted antiferromagnet $YFeO_3$ provides an ideal material system for validating atomic-plane-resolved 3D magnetometry. It crystallizes in the orthorhombic *Pnma* structure (a = 5.302 Å, b = 5.589 Å, c = 7.622 Å) and has three well-defined magnetic anisotropy axes: the [100] a axis is the AFM easy axis and the direction of the Néel vector **L** in the ground state; the [010] b axis is the hard axis; and the [001] c axis is an intermediate axis along which the net DMI-induced canted moment lies (Fig. 2a)[29,30]. Atomic-resolution structural and compositional measurements along the [100] and [010] zone axes confirm the *Pnma* model and chemical ordering (Fig. 2b and Extended Data Figs. 1 and 2). This experimentally validated model supplies the atomic coordinates used, together with crystal symmetry, to constrain the local DMI vectors $\mathbf{D}_{ij}$ in the subsequent energy analysis[31,32]. In the [100]-oriented geometry, the antiparallel magnetization vectors $\mathbf{M}_A$ and $\mathbf{M}_B$ are nearly parallel and antiparallel, respectively, to the incident beam direction z, making $M_z(E)$ the dominant component. The antiferromagnetically coupled Fe(022) planes are separated by 2.25 Å. To investigate field-induced SR, a 3BC tilted from the [100] zone axis was chosen. An external 2.5-T magnetic field applied in the TEM along the [15, 1, $\bar{1}$]direction close to the easy a axis, is expected to result in rotation of the Néel vector towards the [001] c axis, that is, the intermediate anisotropy axis, confined in the ac plane due to magnetic anisotropy.

https://doi.org/10.1038/s41565-026-02270-6

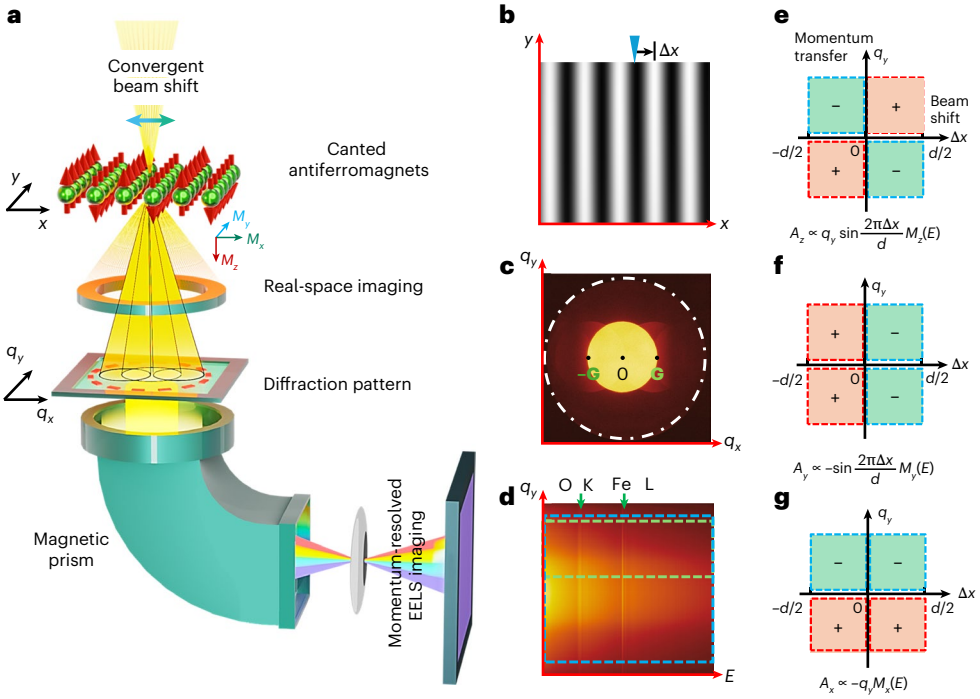


Fig. 1 | Beam-shift-based 4D EMCD for atomic-plane-resolved 3D magnetization mapping. a, A convergent electron beam with controlled beam shift Δx is scanned across antiferromagnetically coupled atomic planes with interplanar distance d on the spin sublattices of a canted antiferromagnet in a 3BC with the **G** systematic reflections excited. **b**,**d**, Real space ADF STEM image in two dimensions (x and y) (**b**) and momentum-resolved EELS in two dimensions (q_y and E) in a 4D EMCD dataset (**d**). **c**, Representative diffraction pattern of a sample in a 3BC with the q_x and q_y axes parallel and perpendicular, respectively, to the **G** vector corresponding to atomic planes with AFM coupling. **e**–**g**, Three different analysis strategies A_z (**e**), A_y (**f**) and A_x (**g**), involving subtraction of EMCD signals acquired in the positive boxes (pink) from those acquired in the negative boxes (green) to extract EMCD spectra that largely represent the $M_z(E)$, $M_y(E)$ and $M_x(E)$ components, respectively, from one 4D EMCD dataset. The theoretical dependences of the analysis strategies on momentum transfer q_y and on a beam-shift-related term $\sin\frac{2\pi\Delta x}{d}$ are shown.

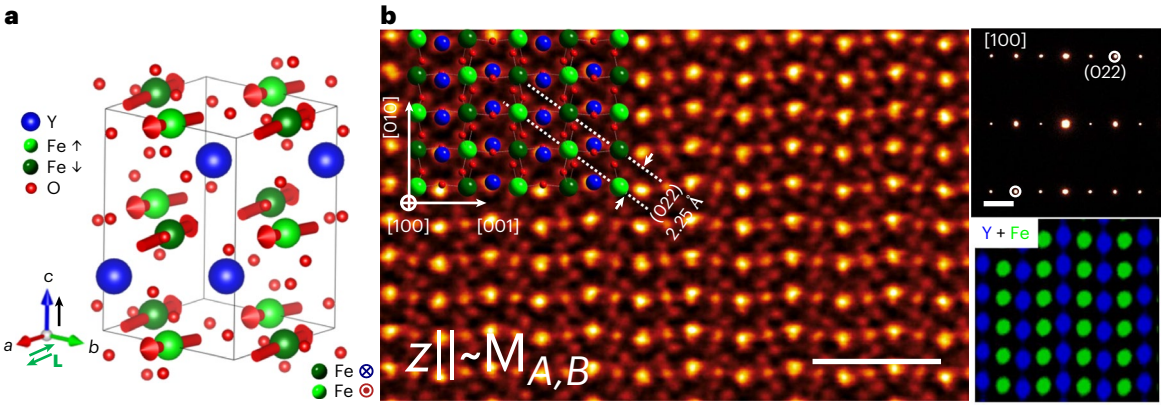


Fig. 2 | Crystal structure, magnetic ground state and atomic-scale characterization of $YFeO_3$. a, Crystal structure and magnetic structure of $YFeO_3$, with magnetic moments indicated by parallel and antiparallel red arrows, respectively, to the [100] a axis. **L** denotes the AFM Néel vector. **b**, Annular bright-field STEM image recorded along the [100] zone axis, revealing the atomic positions of yttrium, iron and oxygen, shown together with a corresponding projected structure model, a selected-area electron diffraction (SAED) pattern and atomic-resolution elemental mapping of yttrium and iron. Scale bars, 1 nm (STEM image), 2 nm^{-1} (SAED pattern).

Dynamical diffraction simulations were performed for $YFeO_3$ under the 3BC with $\mathbf{G}_{(022)}$ excited (Fig. 3a and Extended Data Fig. 3a). A G-type AFM model tentatively assigned opposite M_x, M_y and M_z components to adjacent sublattices. This model was not used to introduce prior constraints when solving the experimental spin vectors. With d_{022} = 2.25 Å, planes sampled at $\Delta x = 0$ and $\pm d_{022}$ carry antiparallel moments. The simulated relative dynamical EMCD coefficient (RC_{emcd}) reproduces the predicted parity in Δx and q_y for $M_z(E)$ (Fig. 3b), $M_y(E)$ (Fig. 3c) and $M_x(E)$ (Fig. 3d). Exploiting these symmetries, the A_z, A_y and A_x combinations isolate signals dominated by $M_z(E)$, $M_y(E)$ and $M_x(E)$, respectively. The simulated target-component fractions are 92.9%, 90.7% and 82.4%, while 88.8%, 84.9% and 95.0% of the corresponding signals originate from the target atomic plane (Extended Data Fig. 3h,k). Thus, a single dataset provides component-selective, plane-localized observables without assuming the actual spin direction. Integration windows and residual cross-talk are detailed in Supplementary Information, section 1.1. We note that these same analysis strategies are equally applicable

https://doi.org/10.1038/s41565-026-02270-6

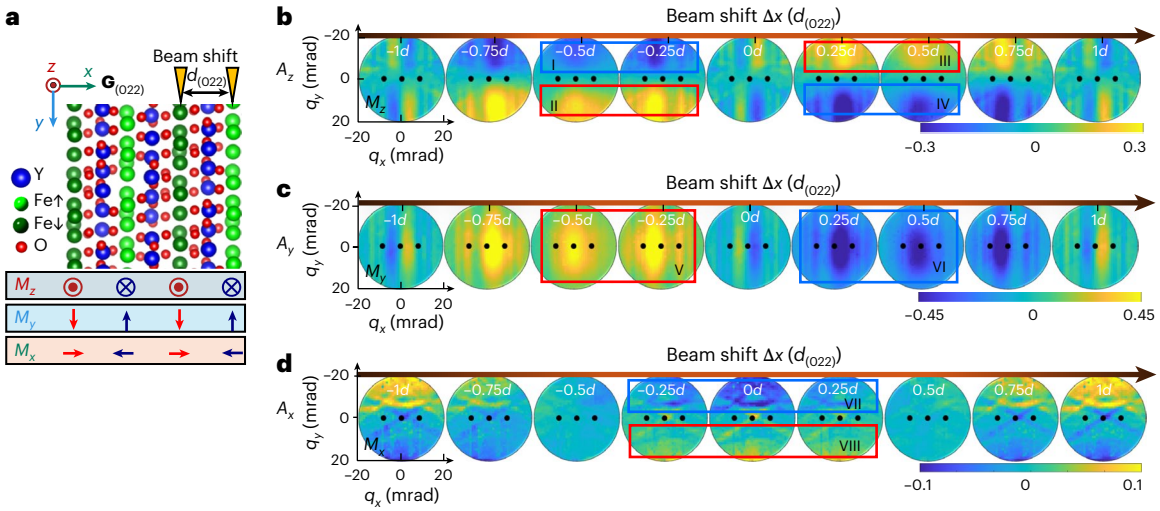


Fig. 3 | Simulated component selectivity of beam-shift-based 4D EMCD. **a**, Top view of a structural model of $YFeO_3$ tilted from [100] to a 3BC with the $\mathbf{G}_{(022)}$ systematic reflections excited in a Cartesian coordinate system with the *x* direction along $\mathbf{G}_{(022)}$ perpendicular to (022) planes with AFM coupling. The incident electron beam in the *z* direction scans along the *x* direction, as indicated by the yellow cones and arrow. **b**–**d**, Beam-shift-dependent distributions of the relative dynamical diffraction coefficient of EMCD (RC_{emcd}) of $M_z(E)$ (**b**), $M_y(E)$ (**c**) and $M_x(E)$ (**d**) along the q_x and q_y directions in the diffraction plane as a function of beam shift Δx from $-1\,d_{(022)}$ to $1\,d_{(022)}$ with a step of $0.25\,d_{(022)}$. Following the theoretical predictions in Fig. 1e–g and equation (1), three analysis strategies, A_z, A_y and A_x, were implemented to largely isolate $M_z(E)$, $M_y(E)$ and $M_x(E)$, respectively, while minimizing their mutual cross-talk. For the three strategies, EMCD signals acquired in the positive red boxes (labelled II and III, V, and VIII, respectively) were subtracted from those acquired in the negative blue boxes (labelled I and IV, VI, and VII, respectively). The three black dots in each beam-shift-dependent distribution of RC_{emcd} denote the centre positions of the $\mathbf{G}_{(0\bar{2}2)}$, transmitted beam and $\mathbf{G}_{(022)}$ disks.

to the complementary [010] geometry in the control experiments (see Supplementary Information, section 2 for details).

Determination of atomic-plane-resolved 3D magnetization vectors

Using the geometry in Fig. 1 and the conditions optimized in Fig. 3, we acquired a 4D EMCD dataset from $YFeO_3$ under a 3BC tilted from [100] with $\mathbf{G}_{(022)}$ excited. The simultaneously recorded ADF STEM image resolves 10 consecutive atomic planes with an interplanar spacing of 2.25 Å, as expected for (022) planes (Fig. 4a). Energy-dispersive X-ray spectroscopy (EDS) mapping and image simulation confirms that the yttrium atomic planes (blue) align with the bright lines, and the iron atomic planes (green) are assigned to the dark lines (Extended Data Fig. 4a,c). The $\mathbf{G}_{(022)}$ disk is parallel to q_x (Fig. 1c), enabling q_y-resolved electron energy-loss spectroscopy (EELS) at each probe position. The A_z (Fig. 3b), A_y (Fig. 3c) and A_x (Fig. 3d) analysis strategies are applied without smoothing or filtering. This approach allowed for the extraction of three sets (Extended Data Figs. 5–7) of EMCD spectra in green, positive ('+' in red) and negative ('−' in blue) EEL spectra for 10 consecutive Fe(022) atomic planes, which are labelled 1–10 (Fig. 4a).

The A_z-channel spectra, which are dominated by the $M_z(E)$ component, reverse sign between adjacent planes and between spectra summed over the two sublattices (Fig. 4e,f,i,j). Both sublattice sums display the expected opposite signs at the iron L_3 and L_2 edges. Across all 10 planes, the experimental relative strength of EMCD (RS_{emcd}) alternates between positive and negative values (Fig. 4b), providing direct AFM contrast across planes. Sublattice-averaged values are -0.148 ± 0.042 for odd-numbered planes and 0.124 ± 0.028 for even-numbered planes (Fig. 4d), with comparable magnitudes within their uncertainties. The orbital-to-spin magnetic moment ratio (m_L/m_S) of iron atoms on all odd-numbered and even-numbered planes was calculated to be 0.046 (Extended Data Fig. 8d), resulting from the almost-quenched orbital moments of Fe^{3+} ions in $YFeO_3$. Therefore, the experimentally observed EMCD signals mainly come from the contribution of 3D magnetic spin moments, rather than magnetic orbital moments.

In comparison to the pronounced out-of-plane $M_z(E)$ signal, by utilizing the A_y analysis strategy with dominant sensitivity to the $M_y(E)$ component, the EMCD spectrum summed over the odd-numbered spin sublattice (Fig. 4k) shows a weak but observable EMCD signature with opposite signals at the L_3 and L_2 peaks, while the EMCD spectrum summed over the even-numbered spin sublattice (Fig. 4l) shows no discernible EMCD signal. A similar characteristic is also reflected in the EMCD spectra extracted from the individual atomic planes labelled 5 (Fig. 4g) and 6 (Fig. 4h). The RS_{emcd} values of the $M_y(E)$ component on the odd-numbered and even-numbered spin sublattices (Fig. 4c) were calculated to be 0.033 ± 0.025 and -0.003 ± 0.029, respectively (Fig. 4d), which are noticeably different from each other. This difference arises from asymmetric rotation of 3D spin vectors on two AFM spin sublattices during field-induced spin reorientation, as discussed in detail in the following section.

In the principal [100]/$\mathbf{G}_{(022)}$ geometry, the A_x-channel spectra show no systematic sign alternation (Extended Data Fig. 7). The sublattice-averaged RS_{emcd} values, -0.022 ± 0.051 for odd-numbered planes and -0.006 ± 0.037 for even-numbered planes, indicate negligible $M_x(E)$ components. A_x sensitivity was independently tested in the complementary [010]/$\mathbf{G}_{(202)}$ geometry, in which the moments project strongly onto the *x* and *y* axes. Both A_x and A_y show sign-reversing contrast between the AFM sublattices, whereas the A_z-derived $M_z(E)$ signal is statistically insignificant (Extended Data Fig. 9). This behaviour agrees with the projected magnetic structure and supports sensitivity to in-plane $M_x(E)$ and $M_y(E)$. Full control data are provided in Supplementary Information, section 2 and Supplementary Figs. 2–6. All component-selective spectra and RS_{emcd} values reported here are direct experimental observables; simulations are subsequently used to determine intrinsic 3D spin vectors.

Simulation-assisted determination of 3D spin vectors

To determine atomic-plane-resolved 3D spin vectors, we used dynamical diffraction simulations to construct a linear system relating the experimental EMCD spectra ($S_+ - S_-$) to the intrinsic $M_z(E)$ and $M_y(E)$

https://doi.org/10.1038/s41565-026-02270-6

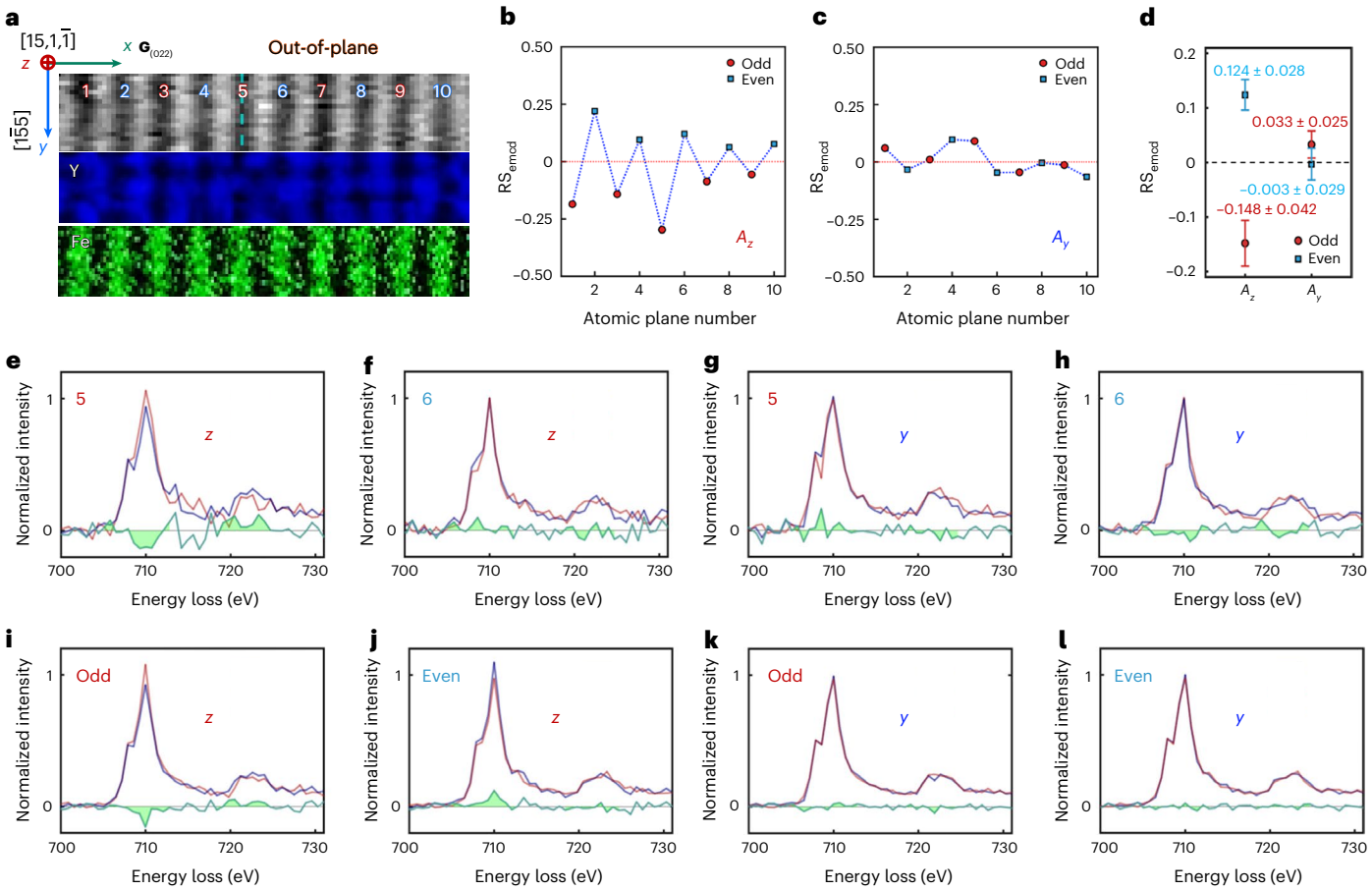


Fig. 4 | 3D vector magnetometry with atomic-plane resolution. **a**, Atomic-resolution ADF STEM image and compositional maps (Y, blue; Fe, green) of $YFeO_3$ in a 3BC with the $\mathbf{G}_{(022)}$ systematic reflections excited in the experimental Cartesian coordinate system with x along $\mathbf{G}_{(022)}$, y along $[1\bar{5}5]$ and z along $[15,1,\bar{1}]$. The corresponding 10 Fe(022) atomic planes are labelled 1–10. **b**,**c**, Experimental relative strength of EMCD (RS_{emcd}) profiles extracted using the A_z (**b**) and A_y (**c**) analysis across the 10 consecutive atomic planes. **d**, Statistical analysis results. Symbols indicate arithmetic means and error bars represent the s.e.m. across five odd-numbered planes (planes 1, 3, 5, 7, 9; $n = 5$ spatial observations) or five even-numbered planes (planes 2, 4, 6, 8, 10; $n = 5$ spatial observations) for each magnetic component. **e**–**l**, Raw data for positive EEL spectra (red), negative EEL spectra (blue) and EMCD spectra (green) for the out-of-plane $M_z(E)$ (**e**,**f**,**i**,**j**) and in-plane $M_y(E)$ (**g**,**h**,**k**,**l**) components of two consecutive Fe(022) atomic planes labelled 5 (**e**,**g**) and 6 (**f**,**h**), and two spin sublattices with all odd-numbered (022) planes (**i**,**k**) and all even-numbered (022) planes (**j**,**l**). The results demonstrate AFM coupling between iron atoms in adjacent (022) planes along the z direction, while the difference in RS_{emcd} for $M_y(E)$ between the two spin sublattices indicates their asymmetric rotation during field-induced spin reorientation.

components, while accounting for cross-talk from adjacent planes and other magnetic components (Extended Data Fig. 10 and Supplementary Information, section 1.1, equations (22)–(26)). The single unique solution for the intrinsic $M_z(E)$ and $M_y(E)$ components can be guaranteed and calculated from this system with the same number of equations and unknowns. It is worth noting that a reconstruction algorithm is not applied here, unlike other tomographic approaches to solving 3D magnetization vectors[14,16]. The robustness of the simulation-assisted determination of 3D spin vectors is discussed in Supplementary Information, section 3 and Supplementary Fig. 7. Accordingly, we are able to investigate spin reorientation in $YFeO_3$ examined in a 3BC tilted away from the [100] zone axis in the presence of an external 2.5-T magnetic field. The RS_{emcd} values of the intrinsic $M_z(E)$ and $M_y(E)$ components are proportional to the projected strengths of 3D magnetic spin moments along the z and y directions, respectively, in the experimental Cartesian coordinate system, which can be converted into the crystallographic coordinate system (Extended Data Fig. 3a). The negligible $M_x(E)$ component is not considered here. The crystallographic directions of the magnetic spin moments $\mathbf{M}_A$ and $\mathbf{M}_B$ on each spin sublattice are determined to be approximately $[9, 1, \bar{1}]$ and $[\bar{5}\bar{1}1]$, respectively (Fig. 5a). The 3D spin vectors $\mathbf{S}$ on each spin sublattice (Fig. 5a) and each atomic plane (for example, planes 1–3; Fig. 5c) are derived from $\mathbf{S} = S\hat{\mathbf{n}}$, where the iron spin $S = 5/2$ in the canted antiferromagnet $YFeO_3$ (ref. 32), and $\hat{\mathbf{n}}$ is the unit vector along the direction of the magnetic spin moments on each spin sublattice and each atomic plane (see Supplementary Information, section 1.3 for details). The angles between the a axis and the 3D spin vectors of the even-numbered and odd-numbered spin sublattice are labelled α and β, respectively. In the zero-field ground state, these angles α_0 and β_0 can be calculated theoretically to be ±1° (Fig. 5a), which is consistent with the experimentally measured angles of approximately ±0.7° (ref. 33). In the presence of an external magnetic field of 2.5 T, the asymmetric SR angles α for $\mathbf{M}_A$ of $[9, 1, \bar{1}]$ and β for $\mathbf{M}_B$ of $[\bar{5}\bar{1}1]$ on each spin sublattice are determined to be 11.6° ± 8.0° from [100] and 19.5° ± 8.2° from $[\bar{1}00]$, respectively (Extended Data Fig. 8a). It is worth noting that the error bars for the SR angles predominantly come from the statistical errors of the experimental EMCD spectra, while the effects of uncertainty in dynamical diffraction coefficients are at least one order of magnitude smaller (Supplementary Table 1 and Supplementary Information, section 3). The observation that $\beta_1 > \alpha_1$ highlights a substantial asymmetric spin reorientation. In contrast, a control experiment was performed in the presence of an external 2.5-T magnetic field applied along the $[1,12,\bar{1}]$ direction for $YFeO_3$ in a 3BC tilted by 8° from the [010] b axis, which is the AFM hard axis. The statistically insignificant $M_z(E)$ components on both spin sublattices along

https://doi.org/10.1038/s41565-026-02270-6

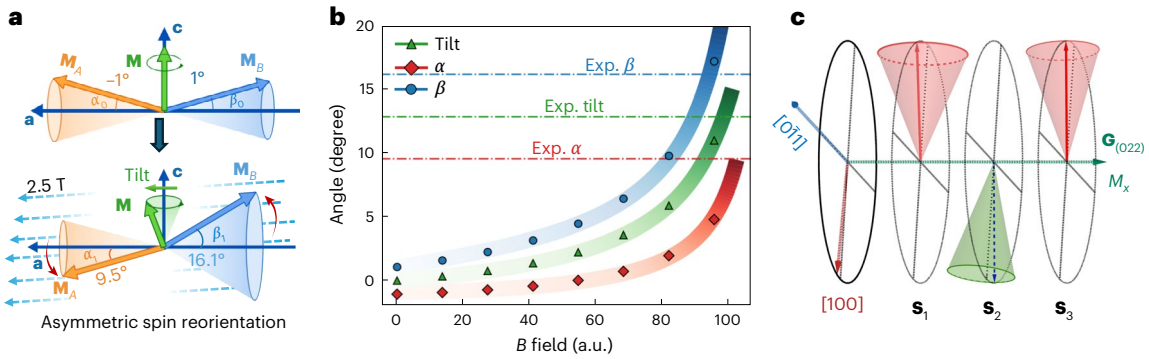


Fig. 5 | Spin Hamiltonian origins of asymmetric spin reorientation in $YFeO_3$. **a**, Schematic diagram showing field-induced asymmetric SR of the magnetic spin moments ($\mathbf{M}_A$ and $\mathbf{M}_B$) for the two spin sublattices viewed along the [010] *b* axis. In the Γ_4 ground state in zero field, the DMI induces canted angles α_0 of −1° and β_0 of 1°, resulting in a net magnetization vector (**M**) along the [001] *c* axis. In a 2.5-T magnetic field, the experimental 3D magnetic spin moments $\mathbf{M}_A$ and $\mathbf{M}_B$ undergo an asymmetric rotation. Their projection onto the *ac* plane yields asymmetric SR angles of $\alpha_1 = 9.5°$ and $\beta_1 = 16.1°$ relative to the *a* axis. **b**, Calculated dependence of the reorientation angles α and β, and the tilting angle of the Néel vector, projected onto the *ac* plane, on an external magnetic field. The calculated asymmetric SR in the two spin sublattices, which is consistent with the experimental observation, arises from competition between the energy contributions, especially from Zeeman energy and SIA, to the spin Hamiltonian. **c**, 3D vectors of the magnetic spin moments $\mathbf{S}_1$, $\mathbf{S}_2$ and $\mathbf{S}_3$ in three consecutive Fe(022) atomic planes labelled 1–3.

Table 1 | Competing spin Hamiltonian energy terms with atomic-plane resolution in $YFeO_3$ with asymmetric spin reorientation in a 2.5-T magnetic field

Atomic plane *i*	$\mathbf{S}_i$	H_{ex}[a]	H_{DM}[a]	H_Z[b]	$H_{sia,a}$[b] (×10^{-3})	$H_{sia,c}$[b] (×10^{-3})
		$-\frac{1}{2}J_{ij}(\mathbf{S}_i \cdot \mathbf{S}_j)$	$\frac{1}{2}\mathbf{D}_{ij} \cdot (\mathbf{S}_i \times \mathbf{S}_j)$	$-\mu_B\mu_0 H\mathbf{H} \cdot \mathbf{S}_i$	$-K_a S_{ia}^2$	$-K_c S_{ic}^2$
1	[−2.31, −0.56, 0.77]	−29.22	0.32	1.257	−27.8	−2.6
2	[2.40, 0.41, −0.57]			−1.285	−29.9	−1.4
3	[−2.39, −0.43, 0.59]	−29.37	−0.03	1.283	−29.8	−1.5
Odd	[−2.36, −0.49, 0.68]	−29.09	−0.43	1.271	−28.8	−2.0
Even	[2.45, 0.29, −0.41]			−1.368	−31.2	−0.7

[a]meV per atom pair. [b]meV per atom.

the [1,12,$\bar{1}$] direction (see Supplementary Information, section 2 for details) further confirm that there is no obvious spin rotation towards the external field direction close to the AFM hard axis, which is consistent with the theoretical expectation due to magnetic anisotropy.

Inference of spin Hamiltonian energy terms

To quantitatively understand the energetic origin of asymmetric spin reorientation, we evaluated the competition between the different energy contributions to the spin Hamiltonian *H* of canted AFM $YFeO_3$ under an applied field using the following established form[32]:

$$\begin{aligned} H &= H_{ex} + H_{DM} + H_Z + H_{sia,a} + H_{sia,c} \\ &= -\frac{1}{2}\sum_{i,j} J_{ij}(\mathbf{S}_i \cdot \mathbf{S}_j) + \frac{1}{2}\sum_{i,j}\mathbf{D}_{ij} \cdot (\mathbf{S}_i \times \mathbf{S}_j) \\ &\quad -\mu_B\mu_0 H\sum_i \mathbf{H} \cdot \mathbf{S}_i - K_a\sum_i S_{ia}{}^2 - K_c\sum_i S_{ic}{}^2, \end{aligned} \tag{2}$$

where H_{ex}, H_{DM}, H_Z, $H_{sia,a}$ and $H_{sia,c}$ are the Hamiltonians of the superexchange interaction, the DMI, the Zeeman energy and the SIA, favouring spin along the *a* and *c* axes, respectively, $\mathbf{S}_i$ and $\mathbf{S}_j$ are two neighbouring spins, while J_{ij} and $\mathbf{D}_{ij}$ are the symmetric superexchange constant and asymmetric DMI vector, respectively. The factor 1/2 avoids double counting. K_a and K_c denote the anisotropy constants along the crystallographic *a* and *c* axes, respectively, while the variables S_{ia} and S_{ic} refer to the projections of the spin vector $\mathbf{S}_i$ onto the *a* and *c* axes, respectively, in $YFeO_3$. All of the spin Hamiltonian energy terms listed in Table 1 are inferred from the 3D spin vectors **S** determined from individual atomic planes and spin sublattices (Table 1 and Supplementary Table 2) and the spin Hamiltonian constants measured from the single-crystalline bulk materials[32] (Supplementary Table 3) according to equation (2). The H_{ex} and H_{DM} energies on the two spin sublattices are inferred to be −29.09 ± 1.33 and −0.43 ± 0.51 meV per atom pair, respectively, while the H_Z energies for each spin sublattice are determined to be 1.271 ± 0.007 and −1.368 ± 0.050 meV per atom. The $H_{sia,a}$ energies for each spin sublattice are $-28.8 \pm 1.0 \times 10^{-3}$ and $-31.2 \pm 2.0 \times 10^{-3}$ meV per atom, which is substantially larger than the $H_{sia,c}$ energies for each spin sublattice of $-2.0 \pm 0.7 \times 10^{-3}$ and $-0.7 \pm 1.0 \times 10^{-3}$ meV per atom, demonstrating a strong energetic preference for spins to align along the *a* axis rather than the *c* axis in the *ac* plane. (see Supplementary Information, section 1.4 for details). Moving beyond the sublattice average, The H_{ex} and H_{DM} energies of each pair of adjacent atomic planes (for example, numbers 1 and 2, numbers 2 and 3), and the H_Z, $H_{sia,a}$ and $H_{sia,c}$ energies for each atomic plane (for example, number 1 to number 3) were calculated and are tabulated in Table 1, enabling statistical analysis and error estimation of the energetic landscape of the spin Hamiltonian at the single-atom-layer limit. From the perspective of the spin Hamiltonian, the observed asymmetric SR angles of the magnetic spin moments on the two spin sublattices arise primarily from the combined effects of opposite H_Z energies (leading to both magnetic spin moments being aligned with the external magnetic field) and H_{sia} energies (favouring the spins to be aligned to the *a* axis in the *ac* plane).

To further elucidate the origin of this asymmetry in SR, density functional theory (DFT) calculations for $YFeO_3$ including the Zeeman term were performed for a field applied 3.8° from the [100] a axis. The calculated field evolution in the ac plane gives different trajectories for α and β (Fig. 5b), qualitatively matching the experimental projected angles of 9.5° ± 6.9° and 16.1° ± 7.8°, respectively. The measured 12.8° tilt angle of the AFM axis is approximately consistent with the 16.1° and 16.5° tilt angles obtained by previous Mössbauer measurements[34] and theoretical calculations[35], respectively, considering the angular errors in our experiments[34,35]. This theoretical calculation also supports the fact that the asymmetric SR angles of the magnetic spin moments on the two spin sublattices are intrinsic to the competition between the four energy contributions, in particular H_Z and H_{sia}, to the spin Hamiltonian in this system.

Conclusions

We have established beam-shift-based 4D EMCD as a platform for atomic-scale 3D vector magnetometry that links inferred spin Hamiltonian energy contributions (H_{ex}, H_{DM}, H_Z, H_{sia}) to local atomic configurations. With dynamical diffraction simulations, a single fixed-orientation acquisition yields atomic-plane-resolved 3D spin vectors, enabling H_{ex} and H_{DM} to be inferred between adjacent planes and H_Z and H_{sia} for individual atomic planes. The spatial resolution of 3D magnetization-vector determination reaches 2.25 Å, inferring atomic-plane-level spin Hamiltonian energy terms. The measured central values indicate an asymmetric reorientation trend between the two AFM sublattices, which is qualitatively supported by theory and interpreted within the spin Hamiltonian framework. Opposite Zeeman contributions and single-ion anisotropy provide a quantitative explanation for the different SR angles, with both sublattice moments rotating within the ac plane in response to the applied field. Our method can be generally applied to different magnetic orderings in canted/collinear antiferromagnets, ferromagnets, helical magnets, and even altermagnets, especially considering that the investigated $YFeO_3$ has altermagnetic symmetry[35,36]. Overall, the approach combines an experimental platform for atomic-scale 3D spin-vector measurements with a theoretical framework for plane-resolved inference of spin Hamiltonian energy contributions. It therefore provides a basis for investigating and ultimately engineering competing magnetic interactions in materials with complex 3D spin order.

Online content

Any methods, additional references, Nature Portfolio reporting summaries, source data, extended data, supplementary information, acknowledgements, peer review information; details of author contributions and competing interests; and statements of data and code availability are available at https://doi.org/10.1038/s41565-026-02270-6.

References

1. Fernández-Pacheco, A. et al. Three-dimensional nanomagnetism. *Nat. Commun.* **8**, 15756 (2017).
2. Coey, J. M. *Magnetism and Magnetic Materials* (Cambridge Univ. Press, 2010).
3. Nagaosa, N. & Tokura, Y. Topological properties and dynamics of magnetic skyrmions. *Nat. Nanotechnol.* **8**, 899–911 (2013).
4. Baltz, V. et al. Antiferromagnetic spintronics. *Rev. Mod. Phys.* **90**, 015005 (2018).
5. Zhou, Y. et al. Dynamically stabilized magnetic skyrmions. *Nat. Commun.* **6**, 8193 (2015).
6. Wang, X., Qaiumzadeh, A. & Brataas, A. Current-driven dynamics of magnetic hopfions. *Phys. Rev. Lett.* **123**, 147203 (2019).
7. Lucassen, J. et al. Stabilizing chiral spin structures via an alternating Dzyaloshinskii–Moriya interaction. *Phys. Rev. B* **102**, 014451 (2020).
8. Sergienko, I. A. & Dagotto, E. Role of the Dzyaloshinskii–Moriya interaction in multiferroic perovskites. *Phys. Rev. B* **73**, 094434 (2006).
9. Boventer, I. et al. Room-temperature antiferromagnetic resonance and inverse spin-Hall voltage in canted antiferromagnets. *Phys. Rev. Lett.* **126**, 187201 (2021).
10. Donnelly, C. et al. Three-dimensional magnetization structures revealed with X-ray vector nanotomography. *Nature* **547**, 328–331 (2017).
11. Hrabec, A. et al. Measuring and tailoring the Dzyaloshinskii–Moriya interaction in perpendicularly magnetized thin films. *Phys. Rev. B* **90**, 020402 (2014).
12. Dmitrienko, V. E. et al. Measuring the Dzyaloshinskii–Moriya interaction in a weak ferromagnet. *Nat. Phys.* **10**, 202–206 (2014).
13. Tanigaki, T. et al. Electron holography observation of individual ferrimagnetic lattice planes. *Nature* **631**, 521–525 (2024).
14. Wolf, D. et al. Unveiling the three-dimensional magnetic texture of skyrmion tubes. *Nat. Nanotechnol.* **17**, 250–255 (2022).
15. Phatak, C., Petford-Long, A. K. & De Graef, M. Three-dimensional study of the vector potential of magnetic structures. *Phys. Rev. Lett.* **104**, 253901 (2010).
16. Yasin, F. S. et al. Bloch point quadrupole constituting hybrid topological strings revealed with electron holographic vector field tomography. *Adv. Mater.* **36**, 2311737 (2024).
17. Chen, Z. et al. Lorentz electron ptychography for imaging magnetic textures beyond the diffraction limit. *Nat. Nanotechnol.* **17**, 1165–1170 (2022).
18. Cui, J., Sha, H., Yang, W. & Yu, R. Antiferromagnetic imaging via ptychographic phase retrieval. *Sci. Bull.* **69**, 466–472 (2024).
19. Edström, A., Lubk, A. & Rusz, J. Quantum mechanical treatment of atomic-resolution differential phase contrast imaging of magnetic materials. *Phys. Rev. B* **99**, 174428 (2019).
20. Kohno, Y., Seki, T., Findlay, S. D., Ikuhara, Y. & Shibata, N. Real-space visualization of intrinsic magnetic fields of an antiferromagnet. *Nature* **602**, 234–239 (2022).
21. Schattschneider, P. et al. Detection of magnetic circular dichroism using a transmission electron microscope. *Nature* **441**, 486–488 (2006).
22. Rusz, J. et al. Magnetic measurements with atomic-plane resolution. *Nat. Commun.* **7**, 12672 (2016).
23. Zhong, X. & Li, Z. Atomic scale visualization of magnetic coupling at individual defects in functional materials by spatially resolved electron magnetic circular dichroism. In *2023 IEEE International Magnetic Conference—Short Papers (INTERMAG Short Papers)* 1–2 (IEEE, 2023).
24. Wang, Z. et al. Atomic scale imaging of magnetic circular dichroism by achromatic electron microscopy. *Nat. Mater.* **17**, 221–225 (2018).
25. Ali, H. et al. Visualizing subatomic orbital and spin moments using a scanning transmission electron microscope. *Nat. Mater.* **24**, 1215–1220 (2025).
26. Gubbiotti, G. et al. 2025 roadmap on 3D nano-magnetism. *J. Phys. Condens. Matter* **37**, 143502 (2025).
27. Treves, D. Magnetic studies of some orthoferrites. *Phys. Rev.* **125**, 1843 (1962).
28. Scola, J. et al. Spin reorientation induced by a very high magnetic field in domain-structured $YFeO_3$ films: emergence of perpendicular anisotropy. *Phys. Rev. B* **81**, 174409 (2010).
29. Du Boulay, D., Maslen, E., Streltsov, V. & Ishizawa, N. A synchrotron X-ray study of the electron density in $YFeO_3$. *Acta Crystallogr. B* **51**, 921–929 (1995).

30. Hahn, S. E. et al. Inelastic neutron scattering studies of $YFeO_3$. *Phys. Rev. B* **89**, 014420 (2014).
31. Moskvin, A. Dzyaloshinskii interaction and exchange-relativistic effects in orthoferrites. *J. Exp. Theor. Phys.* **132**, 517–547 (2021).
32. Amelin, K. et al. Terahertz absorption spectroscopy study of spin waves in orthoferrite $YFeO_3$ in a magnetic field. *Phys. Rev. B* **98**, 174417 (2018).
33. Lütgemeier, H., Bohn, H. & Brajczewska, M. NMR observation of the spin structure and field induced spin reorientation in $YFeO_3$. *J. Magn. Magn. Mater.* **21**, 289–296 (1980).
34. Durbin, G., Johnson, C. & Thomas, M. Direct observation of field-induced spin reorientation in $YFeO_3$ by the Mossbauer effect. *J. Phys. C* **8**, 3051–3057 (1975).
35. Das, S. et al. Anisotropic long-range spin transport in canted antiferromagnetic orthoferrite $YFeO_3$. *Nat. Commun.* **13**, 6140 (2022).
36. Šmejkal, L., Sinova, J. & Jungwirth, T. Beyond conventional ferromagnetism and antiferromagnetism: a phase with nonrelativistic spin and crystal rotation symmetry. *Phys. Rev. X* **12**, 031042 (2022).

Publisher's note Springer Nature remains neutral with regard to jurisdictional claims in published maps and institutional affiliations.

Springer Nature or its licensor (e.g. a society or other partner) holds exclusive rights to this article under a publishing agreement with the author(s) or other rightsholder(s); author self-archiving of the accepted manuscript version of this article is solely governed by the terms of such publishing agreement and applicable law.

© The Author(s), under exclusive licence to Springer Nature Limited 2026

[1]TRACE EM Unit, Department of Materials Science and Engineering and Hong Kong Institute for Clean Energy (HKICE), City University of Hong Kong, Kowloon, China. [2]City University of Hong Kong Matter Science Research Institute (Futian), Shenzhen, China. [3]Nanomanufacturing Laboratory (NML), City University of Hong Kong Shenzhen Research Institute, Shenzhen, China. [4]Peter Grünberg Institute, Forschungszentrum Jülich GmbH, Jülich, Germany. [5]Department of Electronic Engineering, The Chinese University of Hong Kong, Shatin, Hong Kong, China. [6]State Key Laboratory of Functional Crystals and Devices, Shanghai Institute of Ceramics, Chinese Academy of Sciences, Shanghai, China. [7]Department of Physics and Astronomy, Uppsala University, Uppsala, Sweden. [8]Ernst Ruska-Centre for Microscopy and Spectroscopy with Electrons, Forschungszentrum Jülich GmbH, Jülich, Germany. [9]These authors contributed equally: Qi Wang, Miao Zhang. ✉e-mail: xzhong25@cityu.edu.hk

Methods

Theory of atomic-scale EMCD imaging of 3D magnetization vectors

To understand the origin of the 3D EMCD signal in our experiments, in particular for mapping 3D magnetization in canted antiferromagnets using controlled beam shifts, we first describe the expressions for the double-differential scattering cross-section (DDCS) and mixed dynamic form factor (MDFF) based on a theoretical framework[37]. Diffraction patterns of materials consist of a transmitted beam with amplitude T_0 and a series of diffracted disks, each with amplitude $T_{\mathbf{G}}$. The assumption that $T_{\mathbf{G}}$ is independent of $\mathbf{k}$ holds well for thin crystals. In addition, for a thin sample, $T_{\mathbf{G}}$ is purely imaginary with a small absolute value ($|T_{\mathbf{G}\neq 0}| \ll 1$), while $T_0 \approx 1$. Following this notation, the DDCS can be expressed in the form

$$\frac{\partial^2\sigma}{\partial E\partial\Omega} = \sum_{\substack{\mathbf{k},\mathbf{k}',\mathbf{G},\mathbf{G}' \\ k_\perp, k'_\perp < \frac{\alpha}{\lambda}}} T_{\mathbf{G}} T^{\star}_{\mathbf{G}'} e^{i(\chi_{\mathbf{k}}-\chi_{\mathbf{k}'})} S(\mathbf{q},\mathbf{q}',E), \tag{3}$$

where $\mathbf{k}$ and $\mathbf{k}'$ describe the wave vector and mirrored wave vectors, respectively, in the convergent electron beams[38]. $T_{\mathbf{G}}$ and $T_{\mathbf{G}'}$ correspond to the amplitudes of diffraction beams with reciprocal-lattice vectors $\mathbf{G}$ and $\mathbf{G}'$, respectively. $\chi_{\mathbf{k}}$ is a phase contribution from the beam shift 'aberrations' $C_{0,1a}$ and $C_{0,1b}$ in Krivanek's notation in terms of a phase ramp $e^{2\pi i\mathbf{k}\cdot(\Delta x,\Delta y)}$. $S(\mathbf{q},\mathbf{q}',E)$ is the total MDFF, which is described by the energy loss E and by the momentum transfers $\mathbf{q} = \mathbf{k}_f - \mathbf{k} - \mathbf{G}$ and $\mathbf{q}' = \mathbf{k}_f - \mathbf{k}' - \mathbf{G}'$.

In a unit cell of the canted AFM $YFeO_3$ in the two spin-sublattice approximation[33], four iron atoms occupy two AFM spin sublattices, which are indexed $I \in \{A,B\}$ with atomic positions $\mathbf{u}_I$. The total MDFF can be written as a sum of all atomic MDFFs $S_I(\mathbf{q},\mathbf{q}',E)$ of iron at different spin sublattices multiplied by phase factors, as listed below:

$$S(\mathbf{q},\mathbf{q}',E) = \sum_{I\in\{A,B\}} e^{i(\mathbf{q}'-\mathbf{q})\cdot\mathbf{u}_I} S_I(\mathbf{q},\mathbf{q}',E), \tag{4}$$

where the atomic MDFF is

$$S_I(\mathbf{q},\mathbf{q}',E) = \sum_{i,f} \left\langle f_I \left| \frac{e^{-2\pi i\mathbf{q}\cdot(\mathbf{r}-\mathbf{u}_I)}}{\mathbf{q}^2} \right| i_I \right\rangle \left\langle i_I \left| \frac{e^{2\pi i\mathbf{q}'\cdot(\mathbf{r}-\mathbf{u}_I)}}{\mathbf{q}'^2} \right| f_I \right\rangle \times \delta(E_{i_I} - E_{f_I} + E), \tag{5}$$

$|i_I\rangle$ and $|f_I\rangle$ are the initial and final states of iron atoms on AFM spin sublattices of $I \in \{A,B\}$ with energies E_{i_I} and E_{f_I}, respectively, and E is the energy loss. In the dipole approximation, the atomic MDFF of iron atoms in the AFM spin sublattices of $I \in \{A,B\}$ separates into non-magnetic and magnetic contributions in the form

$$S_I(\mathbf{q},\mathbf{q}',E) \approx \frac{1}{q^2q'^2}\left[\mathbf{q}\cdot\mathcal{N}_I(E)\cdot\mathbf{q}' + i(\mathbf{q}\times\mathbf{q}')\cdot\mathbf{M}_I(E)\right], \tag{6}$$

where $N_I(E)$ is a real-valued symmetric rank 2 tensor containing information about the non-magnetic part of the electronic structure and $\mathbf{M}_I(E)$ is a magnetization vector containing information about spin and orbital magnetism and the magnetic dipole term of atoms with atomic positions $\mathbf{u}_I$. In pseudo-cubic $YFeO_3$, the rank-2 tensor $\mathcal{N}_I(E)$ is approximated as isotropic, so its contraction with $\mathbf{q}$ and $\mathbf{q}'$ reduces to the scalar term $N_I(E)\mathbf{q}\cdot\mathbf{q}'$, where $N_I(E)$ is the corresponding scalar function, as shown below[39]:

$$S_I(\mathbf{q},\mathbf{q}',E) \approx \frac{1}{q^2q'^2}\left[N_I(E)\mathbf{q}\cdot\mathbf{q}' + i(\mathbf{q}\times\mathbf{q}')\cdot\mathbf{M}_I(E)\right] \tag{7}$$

Substituting equations (7) and (4) into equation (3), the DDCS of the general spectrum of iron in $YFeO_3$ can be rewritten as a linear combination of the non-magnetic component and the magnetic component of the MDFF of the iron atoms on the AFM spin sublattices of $I \in \{A,B\}$:

$$\begin{aligned}\frac{\partial^2\sigma}{\partial E\partial\Omega} = &\sum_{I\in\{A,B\}} N_I(E) \sum_{\substack{\mathbf{k},\mathbf{k}',\mathbf{G},\mathbf{G}' \\ k_\perp, k'_\perp < \frac{\alpha}{\lambda}}} T_{\mathbf{G}} T^{\star}_{\mathbf{G}'} e^{i(\chi_{\mathbf{k}}-\chi_{\mathbf{k}'})} \frac{\mathbf{q}\cdot\mathbf{q}'}{q^2q'^2} e^{i(\mathbf{q}'-\mathbf{q})\cdot\mathbf{u}_I} \\ &+ \sum_{I\in\{A,B\}} \sum_{\substack{\mathbf{k},\mathbf{k}',\mathbf{G},\mathbf{G}' \\ k_\perp, k'_\perp < \frac{\alpha}{\lambda}}} iT_{\mathbf{G}} T^{\star}_{\mathbf{G}'} e^{i(\chi_{\mathbf{k}}-\chi_{\mathbf{k}'})} \frac{(\mathbf{q}\times\mathbf{q}')\cdot\mathbf{M}_I(E)}{q^2q'^2} e^{i(\mathbf{q}'-\mathbf{q})\cdot\mathbf{u}_I}\end{aligned}. \tag{8}$$

This formulation inherently separates the spectrum into a non-magnetic component originating from the real parts of the MDFFs and a magnetic component originating from the imaginary parts of the MDFFs. The latter contribution arises from magnetic dichroism and constitutes the EMCD signal.

In a thin sample, the Bragg discs for non-zero $\mathbf{G}$ have very small amplitudes. We therefore neglect them in a first approximation. Furthermore, summing over atoms in a crystal leads to a condition where $\mathbf{q} - \mathbf{q}'$ and consequently also $\mathbf{k} - \mathbf{k}'$ needs to be a reciprocal-lattice vector. The expression for the magnetic part of the DDCS from an iron atom from spin sublattice 'A' located at the origin, that is, with a basis vector $\mathbf{u}_A = 0$, can then be simplified to the following form:

$$\frac{\partial^2\sigma}{\partial E\partial\Omega}\Big|_{\text{Mag}} \propto \sum_{\substack{\mathbf{k},\mathbf{G} \\ k_\perp < \frac{\alpha}{\lambda}}} \sin\Delta\chi_{\mathbf{k},\mathbf{G}} \frac{M_x(E)(G_yq_z - G_zq_y) + M_y(E)(G_zq_x - G_xq_z) + M_z(E)(G_xq_y - G_yq_x)}{q^2q'^2}, \tag{9}$$

where $\Delta\chi_{\mathbf{k},\mathbf{G}} = \Delta\chi_{\mathbf{k},\mathbf{k}'} = \chi_{\mathbf{k}} - \chi_{\mathbf{k}'} = \chi_{\mathbf{k}} - \chi_{\mathbf{k}+\mathbf{G}}$ is the phase difference between the $\mathbf{k}$ and $\mathbf{k}'$ components of the convergent beam.

In a thicker sample, additional terms are superimposed onto this contribution. However, at a sample thickness of 16.8 or 20 nm, it is reasonable to expect that it will constitute a major contribution to the distribution of the EMCD signal in the diffraction plane, as a function of beam position.

Apart from the contributions that are dependent on beam position through the phase ramp in the wavefunction of the convergent probe, there are also contributions from so-called classical EMCD, which arise from interference of the probe with Bragg-scattered beams. They require non-negligible excitation of the Bragg spots—as in the classical EMCD geometry, in either the two beam orientation[21] or the three-beam orientation used here. In general, any two beams will lead to interference effects. In particular, apart from the systematic row of reflections, in the diffraction patterns other rows of reflections are visible, originating from different Laue zones. As discussed in refs. 37,38, this leads to terms of the form

$$2|T_G|\Im S_I(\mathbf{q},\mathbf{q}') = 2|T_G|\frac{(\mathbf{q}\times\mathbf{q}')\cdot\mathbf{M}(E)}{q^2q'^2}, \tag{10}$$

that is, without an explicit dependence on the phase ramps introduced by the beam shift. Nevertheless, simulations show that even classical EMCD contributions from individual atomic planes have finite extent[40] and their sign follows the direction of the orientation of the magnetic moments.

In the first experimental Cartesian coordinate system of the $YFeO_3$ sample tilted to a 3BC with the (022) systematic reflections excited, the x, y and z directions are defined as $\mathbf{G}_{(022)}$, $[1\bar{5}5]$ and $[15,1,\bar{1}]$, respectively (Fig. 4a and Extended Data Fig. 3a). The corresponding simulated diffraction pattern (Extended Data Fig. 2c) shows a strongly excited $\mathbf{G}_{(022)}$ (encircled by a blue circle) in the zero-order Laue zone (ZOLZ), which is regarded as G_x, while other diffraction spots such as $\mathbf{G}_{(1\bar{4}8)}$ (encircled

by a red circle) in the first-order Laue zone (FOLZ) can also be weakly excited and projected along the G_z and G_y directions, leading to contributions from G_z and G_y components in the first experimental condition.

Similarly, in the second experimental Cartesian coordinate system of the $YFeO_3$ sample tilted to a 3BC with the (202) systematic reflections excited, the x, y and z directions correspond to $\mathbf{G}_{(202)}$, $[9\bar{2}\bar{9}]$ and $[1, 12, \bar{1}]$, respectively (Extended Data Fig. 2b and Extended Data Fig. 9a). Analogously, $\mathbf{G}_{(202)}$ (encircled by a blue circle) in the ZOLZ is dominantly excited as G_x, while other diffraction spots such as $\mathbf{G}_{(\bar{4}\bar{1}7)}$ (encircled by a red circle) in the FOLZ can also be weakly excited and projected along the G_z and G_y directions, leading to contributions from G_z and G_y components in the second experimental condition.

According to the Fourier shift theorem, a controlled beam shift by Δx along the x direction perpendicular to the (022) atomic plane in the first experimental Cartesian coordinate system introduces a position-dependent phase ramp $e^{2\pi i\mathbf{k}\cdot\Delta x}$ in an incident electron beam, resulting in a phase difference of $\Delta\chi_{\mathbf{k},\mathbf{G}} = 2\pi\mathbf{G}\cdot\Delta x$. For $M_y(E)$ and $M_z(E)$, the strongly excited $\mathbf{G}_{(022)}$ as G_x, compared to G_y and G_z, is dominant in the phase difference of $\Delta\chi_{\mathbf{k},\mathbf{G}}$. As a result, $\Delta\chi_{\mathbf{k},\mathbf{G}}$ can be approximated as $\Delta\chi_{\mathbf{k},\mathbf{G}_x} = \sin\frac{2\pi\Delta x}{d}$, where $d = d_{(022)} = 1/G_{(022)}$. For $M_x(E)$, the classical EMCD provides the main contribution. Since G_x and $M_x(E)$ are parallel, the term $(G_x \times \mathbf{q})\cdot M_x(E)$ in equation (9) is zero, demonstrating that only the weakly excited G_z and G_y, rather than the strongly excited G_x, can be used to detect the $M_x(E)$ component. Therefore, the $M_x(E)$ component is detected through the classical EMCD approach described in equation (10). Based on this analysis of the primary sources of $M_x(E)$, $M_y(E)$ and $M_z(E)$, the magnetic component of the DDCS can be approximated as:

$$\begin{aligned}\frac{\partial^2\sigma}{\partial E\partial\Omega}\Big|_{\mathrm{Mag}} &\propto \sum_{\mathbf{k},\mathbf{G}}\Big[2|T_{\mathbf{G}}|\tfrac{G_yq_z-G_zq_y}{q^2q'^2}M_x(E)\\ &+\sin\tfrac{2\pi\Delta x}{d}\tfrac{G_zq_x-G_xq_z}{q^2q'^2}M_y(E)+\sin\tfrac{2\pi\Delta x}{d}\tfrac{G_xq_y-G_yq_x}{q^2q'^2}M_z(E)\Big]\\ &=\sum_{\mathbf{k},\mathbf{G}}\tfrac{1}{q^2q'^2}\begin{vmatrix}G_x & q_x & 2|T_{\mathbf{G}}|M_x(E)\\ G_y & q_y & \sin\frac{2\pi\Delta x}{d}M_y(E)\\ G_z & q_z & \sin\frac{2\pi\Delta x}{d}M_z(E)\end{vmatrix}=\sum_{\mathbf{k},\mathbf{G}}S(\Delta x,\mathbf{q},\mathbf{G},\mathbf{M}(E)),\end{aligned}\tag{11}$$

where $S(\Delta x, \mathbf{q}, \mathbf{G}, \mathbf{M}(E))$ is a single item in the summation formula as a function of Δx, $\mathbf{q}$, $\mathbf{G}$ and $\mathbf{M}(E)$. Typically, the need for reflections outside the systematic row results in a small dynamical coefficient in front of $M_x(E)$, as demonstrated previously[41]. Careful orientation of the sample so that excitations of nearby rows of reflections from higher-order Laue zones are present offers a route to enhance this contribution, as used in this work.

Crystal growth and structural characterization

High-purity polycrystalline raw material powders of Y_2O_3 (99.99%) and Fe_2O_3 (99.99%) were precisely weighed in accordance with the stoichiometric ratio 1:1. The homogenized mixture underwent calcination in a muffle furnace (1,200 °C, 10 h, static air) with controlled cooling (2 °C min^{-1}) to room temperature to ensure phase-pure $YFeO_3$ formation via solid-state reaction. Following calcination, the agglomerated powder was comminuted through secondary ball milling (8 h). The refined powder was uniaxially compacted into cylindrical green bodies (10 mm diameter × 50 mm) using a cold isostatic press (120 MPa, 1-h dwell time). Densification was completed via pressureless sintering (1,250 °C, 24 h, air atmosphere). The fabricated ceramic rods were polished to attain a uniform diameter for subsequent crystal growth procedures.

Single-crystal cultivation was performed in a four-mirror optical floating zone furnace under forced air convection (5 l min^{-1} flow rate). Thermal energy input was provided by four water-cooled quartz-halogen irradiation sources (1.5 kW each). Growth parameters were optimized at a 4 mm h^{-1} translation rate with a counter-rotation protocol (seed rod, 8 r.p.m.; feed rod, 8 r.p.m.) to maintain a stable molten zone geometry. The as-grown $YFeO_3$ boule had dimensions of 5 mm diameter × 40 mm. The crystal structure of $YFeO_3$ was analysed by X-ray diffractometry. Crystal orientations were determined from an X-ray Laue photograph.

Data acquisition and analysis

Atomic-resolution STEM experiments, including ADF STEM imaging, annular bright-field (ABF) STEM imaging and EDS compositional mapping of $YFeO_3$ along zone axis conditions were performed using a double spherical aberration (Cs)-corrected JEOL Grand ARM S/TEM equipped with a cold field emission gun and operated at an accelerating voltage of 300 kV using a convergence semi-angle of 26.5 mrad. ABF STEM images were collected using an annular detector with inner and outer collection semi-angles of 12 and 24 mrad, respectively. ADF STEM images were collected using an annular detector with inner and outer collection semi-angles of 60 and 180 mrad, respectively, while simultaneously performing compositional mapping using STEM EDS.

4D EMCD datasets, ADF STEM images and EDS compositional maps of $YFeO_3$ in a 3BC with the desired $\mathbf{G}$ systematic reflections excited were acquired using a convergence semi-angle of 8.95 mrad at an accelerating voltage of 300 kV. The $YFeO_3$ samples were tilted away from the [100] and [010] zone axes by 7°–8° to achieve 3BCs with the (022) and (202) systematic reflections excited, respectively. In the 4D EMCD datasets, a convergent electron beam was scanned over the $YFeO_3$ sample in a 3BC with the (022) or (202) systematic reflections excited to form momentum-resolved 2D EELS images of q_y and E at each scanning point and a real-space ADF STEM image with dimensions along x and y. A spectrometer entrance aperture with a diameter of 5 mm (corresponding to ~45 mrad) and a dispersion of 0.35 or 0.7 eV per channel were applied, resulting in an energy resolution of ~1 eV. The sample thickness was determined by calibrating the inelastic mean free path (λ) using position-averaged convergent beam electron diffraction and comparisons with multislice simulations. Application of this calibrated value of λ to low-loss EELS spectra yielded thickness values of $t \approx 16.8$ nm and 20 nm for the [100] and [010] acquisition regions, respectively[42]. Detailed data processing and quantitative analysis are shown in Supplementary Fig. 1 and discussed in the Supplementary Information.

Dynamical diffraction simulation and DFT calculation

For a dynamical diffraction simulation of $YFeO_3$ tilted from the [100] zone axis to a 3BC with the (022) systematic reflections excited, an initial supercell with the a axis along $[0\bar{4}\bar{2}]$, the b axis along $[0\bar{1}1]$ and the c axis along [100] was built from an orthorhombic unit cell of $YFeO_3$ in the two spin-sublattice approximation[33]. Here, we ignored the slight monoclinic distortion of this initial supercell and approximated it by an orthogonal cell with lattice constants of a = 13.29 Å, b = 9.40 Å, c = 5.42 Å. The incident beam was tilted from the [100] zone axis by 8°.

For a dynamical diffraction simulation of $YFeO_3$ tilted from the [010] zone axis to a 3BC with the (202) systematic reflections excited, an initial supercell with the a axis along $[\bar{4}0\bar{2}]$, the b axis along $[10\bar{1}]$ and the c axis along [010] was built. Here we also ignored the slight monoclinic distortion of this initial supercell and approximated it by an orthogonal one with lattice constants of a = 13.06 Å, b = 9.28 Å, c = 5.59 Å. The incident beam was tilted from the [010] zone axis by 8°.

To calculate the EMCD signal distribution for $YFeO_3$ in 3BCs with the (022) or (202) systematic reflections excited, as mentioned above, a combined multislice/Bloch-wave method[43] was utilized for a convergence parameter of 1×10^{-4}, a beam convergence semi-angle of 8.95 mrad and an accelerating voltage of 300 kV. The collection semi-angle, which was determined by the radius of the spectrometer entrance aperture, was ~17 mrad and ~20 mrad for 3BCs with the (022) and (202) systematic reflections, respectively, excited. The step size of the beam shifts

was set to 0.125d, where d is the interplanar distance between adjacent (022) or (202) iron atomic planes. All of the parameters that were used in the simulations were consistent with those used in the experiments.

DFT calculations were performed in the local density approximation[44] using the full-potential linearized augmented plane wave (FLAPW) method, as implemented in the FLEUR code[45]. Spin–orbit coupling was taken into account and the local spin directions were allowed to freely relax[46] in an applied field. The crystal structure was chosen according to the experimental data. The basis-function cut-off, K_{mas}, and minimal muffin-tin radii, R_{MT}, were chosen to yield $K_{mas}R_{MT} = 6$, while a $6 \times 5 \times 4$ k-point mesh was used. No Hubbard-U was used for the iron d states, leading to a better description of spin canting[47].

Data availability

Raw experimental data for this study are available via Zenodo at https://doi.org/10.5281/zenodo.21442331 (ref. 48). All other data supporting the findings of this study are included in the Article and its Supplementary Information. Source data are provided with this paper.

References

37. Rusz, J. & Idrobo, J. C. Aberrated electron probes for magnetic spectroscopy with atomic resolution: theory and practical aspects. *Phys. Rev. B* **93**, 104420 (2016).
38. Rusz, J., Idrobo, J.-C. & Bhowmick, S. Achieving atomic resolution magnetic dichroism by controlling the phase symmetry of an electron probe. *Phys. Rev. Lett.* **113**, 145501 (2014).
39. Negi, D. S., Idrobo, J. C. & Rusz, J. Probing the localization of magnetic dichroism by atomic-size astigmatic and vortex electron beams. *Sci. Rep.* **8**, 4019 (2018).
40. Rusz, J. et al. Localization of magnetic circular dichroic spectra in transmission electron microscopy experiments with atomic plane resolution. *Phys. Rev. B* **95**, 174412 (2017).
41. Rusz, J., Rubino, S., Eriksson, O., Oppeneer, P. M. & Leifer, K. Local electronic structure information contained in energy-filtered diffraction patterns. *Phys. Rev. B* **84**, 064444 (2011).
42. Oberaigner, M. et al. Online thickness determination with position averaged convergent beam electron diffraction using convolutional neural networks. *Microsc. Microanal.* **29**, 427–436 (2023).
43. Rusz, J. Modified Automatic Term Selection v2: a faster algorithm to calculate inelastic scattering cross-sections. *Ultramicroscopy* **177**, 20–25 (2017).
44. Vosko, S. H., Wilk, L. & Nusair, M. Accurate spin-dependent electron liquid correlation energies for local spin density calculations: a critical analysis. *Can. J. Phys.* **58**, 1200–1211 (1980).
45. Wortmann, D. et al. Fleur. *Zenodo* https://doi.org/10.5281/zenodo.7576163 (2023).
46. Kurz, P., Förster, F., Nordström, L., Bihlmayer, G. & Blügel, S. Ab initio treatment of noncollinear magnets with the full-potential linearized augmented plane wave method. *Phys. Rev. B* **69**, 024415 (2004).
47. Stoeffler, D. & Chaker, Z. First principles study of the electronic structure and magnetic properties of $YFeO_3$ oxide. *J. Magn. Magn. Mater.* **442**, 255–264 (2017).
48. Wang, Q. & Zhong, X. Source data for atomic resolved 3D magnetic vector. *Zenodo* https://doi.org/10.5281/zenodo.21442331 (2026).

Acknowledgements

F.-R. Chen, T.-F. Hung and Z. Li are gratefully acknowledged for helpful discussions and assistance. This work made use of the resources of the TRACE TEM centre at the City University of Hong Kong.

Author contributions

X.Z. initiated the idea and designed the study. Q.W. and X.Z. conducted the experiments, while M.Z. performed the simulations. Q.W., X.Z. and M.Z. performed the quantitative analysis, with J.L., Y.S. and S.-W.H. contributing to data analysis. G.B. performed the DFT calculation and analysis. A.W., W.D. and L.S. synthesized the materials. J.R. provided support on theoretical simulations and data analysis. R.E.D.-B. contributed to scientific discussion and theoretical explanation. Q.W., M.Z. and X.Z. wrote the initial draft of the paper. All authors participated in reviewing and editing the manuscript.

Funding

This work was financially supported by the GuangDong Basic and Applied Basic Research Foundation (2024A1515012303), the Sino-German Mobility Programme by the Sino-German Center for Research Promotion (M-0265), Innovation and Technology Fund (RAI/23/1/020A), the City University of Hong Kong (project numbers 7020207, 9610484, 9680291, 9678288, 9610607, 7030048) and the City University of Hong Kong Shenzhen Research Institute. The work described in this paper was substantially supported by a grant from the EU-HK Research and Innovation Cooperation Co-funding Mechanism sponsored by the Research Grants Council of Hong Kong Special Administrative Region, China (project number E-CityU101/20), and the Research Grants Council of the Hong Kong Special Administrative Region, China (project number CityU 11307926, C1013-23EF, C1018-22E, CityU 11309822). This project has received funding from the European Research Council (ERC) under the European Union's Horizon 2020 research and innovation programme (grant number 856538, project '3D MAGiC'). This project has been funded by the Deutsche Forschungsgemeinschaft (DFG, German Research Foundation) – Project-ID 405553726 – TRR 270. J.L. acknowledges financial support from the National Natural Science Foundation of China (project number T2422017) and the Hong Kong Research Grants Council (21204124). A.W., W.D. and L.S. acknowledge financial support from the National Natural Science Foundation of China (project number 52272014, W2421113), the International Partnership Program of Chinese Academy of Sciences (number 030GJHZ2024093MI), the Self-developed Key Project of State Key Laboratory of Functional Crystals and Devices (GNJT-2025-ZD05) and the CAS Project for Young Scientists in Basic Research (YSBR-024). J.R. acknowledges the support of the Swedish Research Council (grant number 2021-03848), the Olle Engkvist Foundation (grant number 214-0331), STINT (grant number CH2019-8211) and the Knut and Alice Wallenberg Foundation (grant number 2022.0079). G.B. gratefully acknowledges computing time granted through JARA-HPC on the supercomputer JURECA at Forschungszentrum Jülich.

Competing interests

The authors declare no competing interests.

Additional information

Extended data is available for this paper at https://doi.org/10.1038/s41565-026-02270-6.

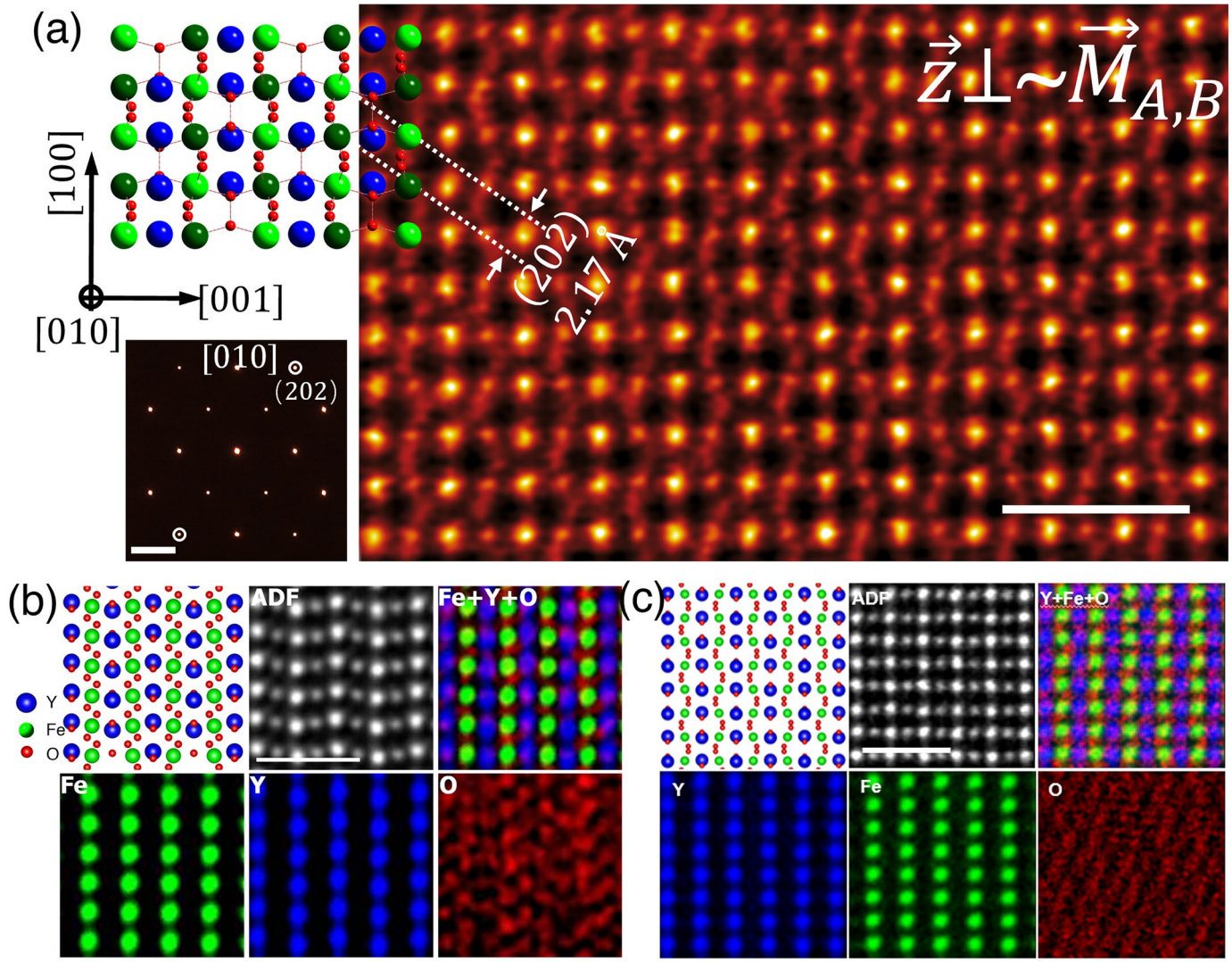
Supplementary information The online version contains supplementary material available at https://doi.org/10.1038/s41565-026-02270-6.

Correspondence and requests for materials should be addressed to Xiaoyan Zhong.

Peer review information *Nature Nanotechnology* thanks the anonymous reviewers for their contribution to the peer review of this work. Peer reviewer reports are available.

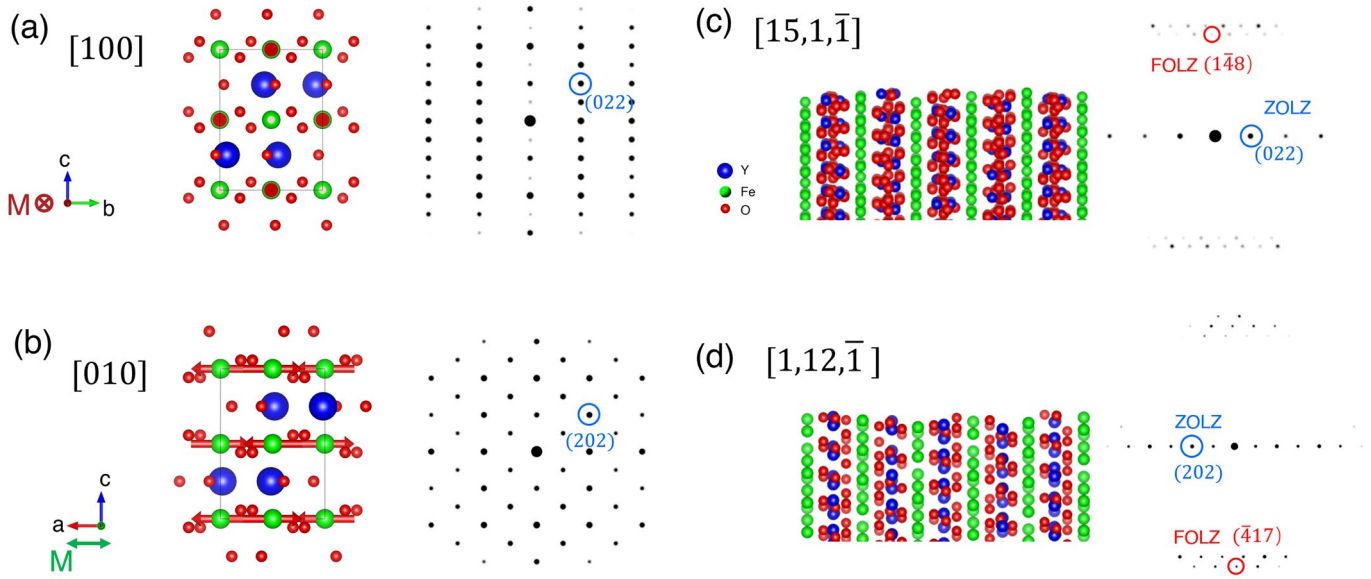
Reprints and permissions information is available at www.nature.com/reprints.

https://doi.org/10.1038/s41565-026-02270-6



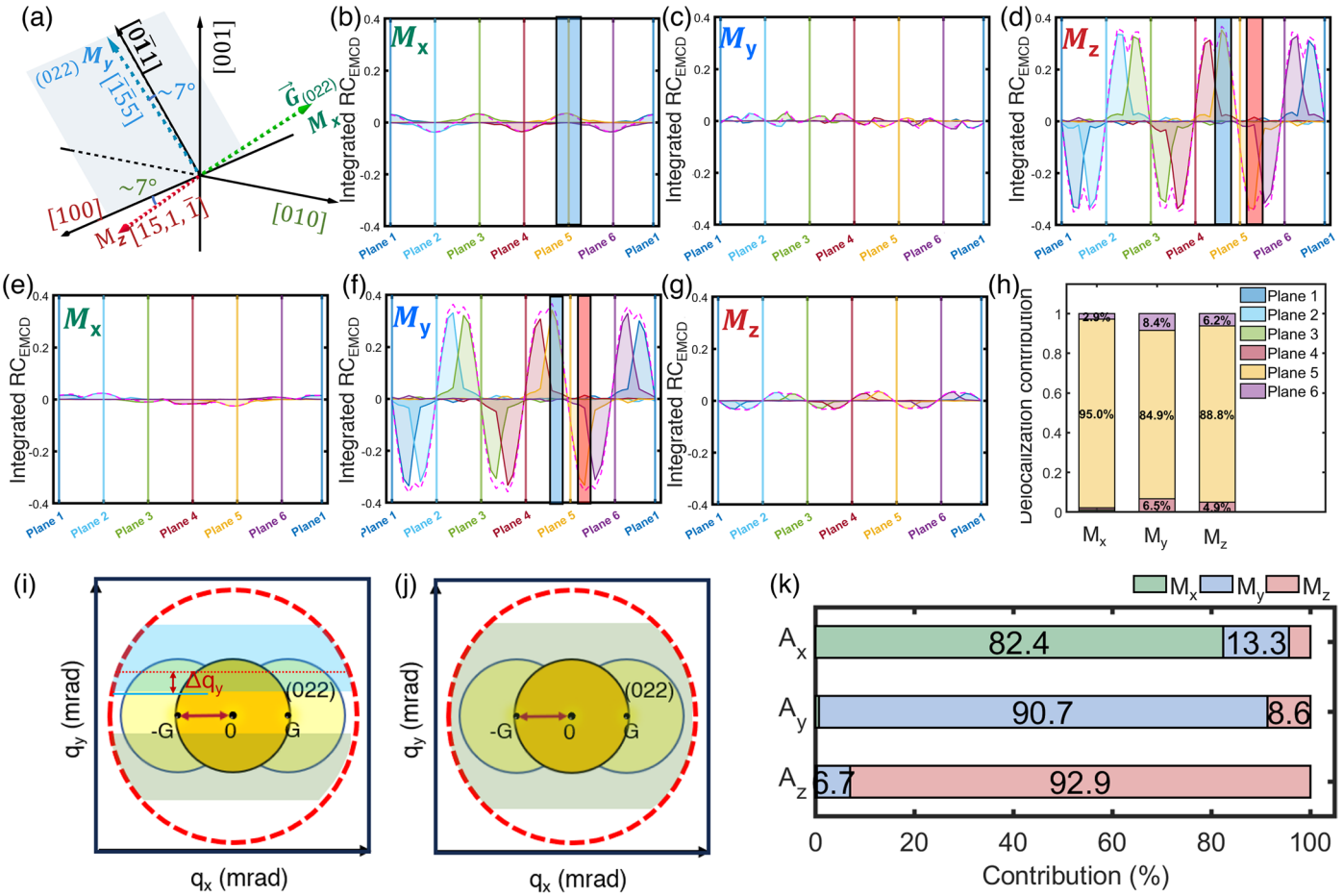
Extended Data Fig. 1 | Atomic-resolution structural and compositional characterization of YFeO3. (**a**) Annular bright-field (ABF) scanning transmission electron microscopy (STEM) image recorded along the [010] zone axis, revealing the atomic positions of Y, Fe and O, together with a corresponding projected structure model, a selected area electron diffraction (SAED) pattern, annular dark-field (ADF) STEM images and corresponding atomic-resolution elemental maps of Y in blue and Fe in green along [100]. Scale bars on all STEM images are 1 nm and on diffraction patterns are 2 1/nm. (**b-c**) Projected structural models, atomic-resolution ADF STEM images and compositional maps showing Fe in green, Y in blue and O in red for $YFeO_3$ viewed along (**b**) [100] and (**c**) [010].

https://doi.org/10.1038/s41565-026-02270-6



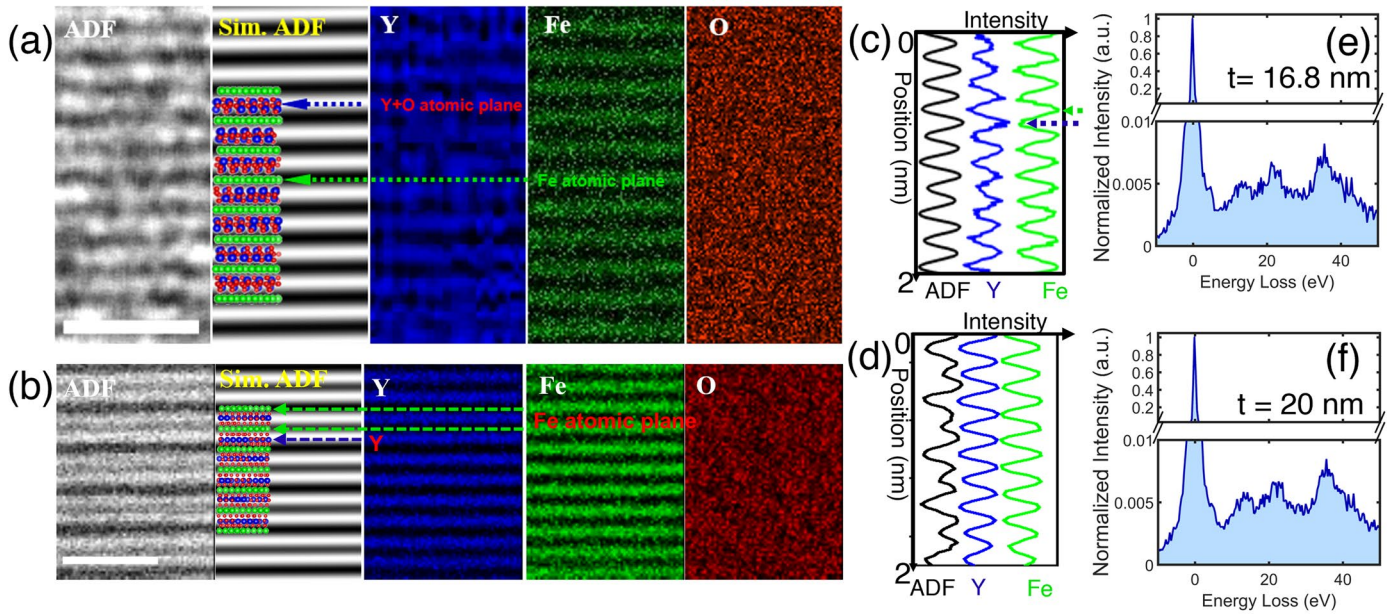
Extended Data Fig. 2 | Projected magnetic structures and diffraction geometries of $YFeO_3$. Projected structural models with magnetization vectors marked using arrows and simulated selected area electron diffraction patterns for $YFeO_3$ viewed along (**a**) [100], (**b**) [010], (**c**) [15,1, $\bar{1}$] and (**d**) [1,12, $\bar{1}$]. [15,1, $\bar{1}$] and [1,12, $\bar{1}$] represent the crystallographic orientations of $YFeO_3$ in a three-beam condition with the $\mathbf{G}_{(022)}$ and $\mathbf{G}_{(202)}$ systematic reflections excited, respectively. Blue circles mark strongly excited (202) and (022) diffraction spots in the zero-order Laue zone (ZOLZ), while red circles mark diffraction spots such as (1$\bar{4}$8) and ($\bar{4}$17) in the first-order Laue zone (FOLZ).

https://doi.org/10.1038/s41565-026-02270-6



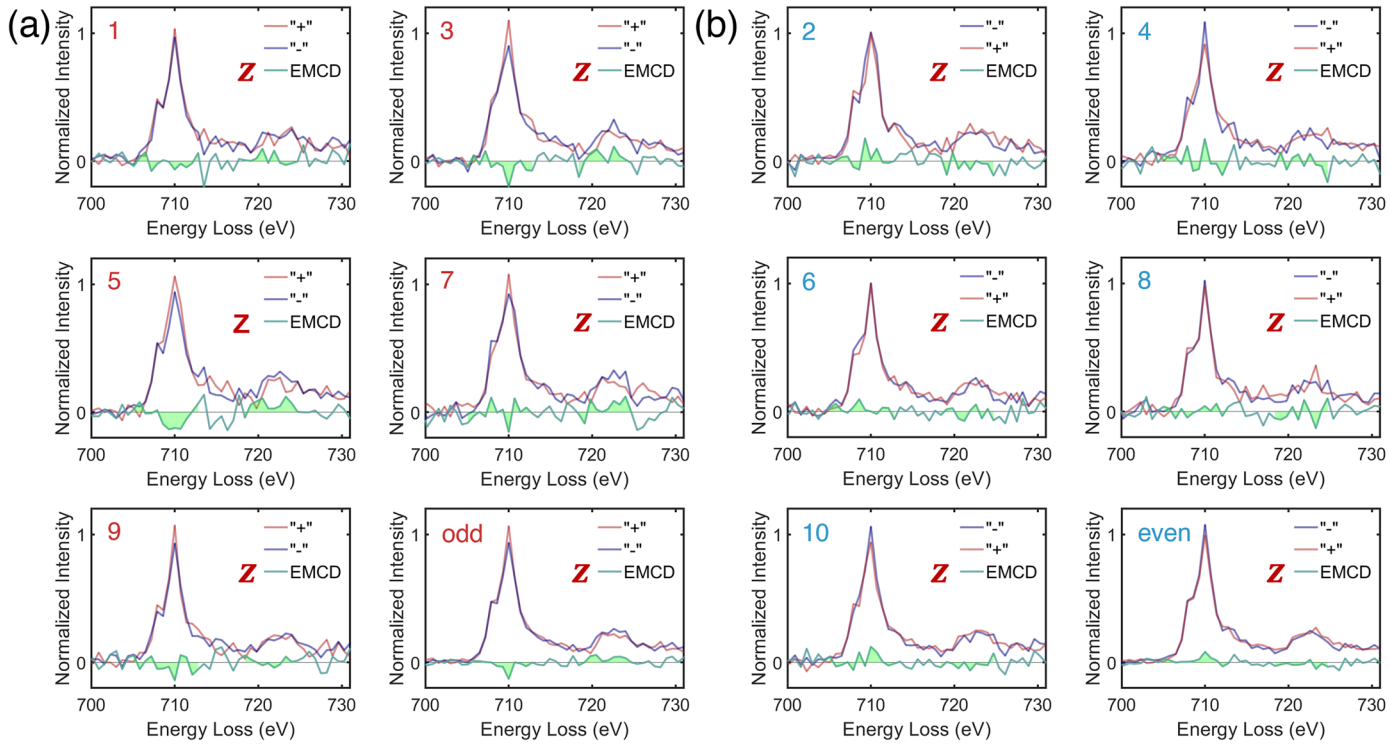
Extended Data Fig. 3 | Beam-shift dependence and component selectivity of simulated three-dimensional EMCD signals. Beam-shift-dependent profiles of integrated relative dynamical diffraction coefficient of electron magnetic circular dichroism (RC_{emcd}) of three-dimensional (3D) magnetization vectors. (**a**) First experimental Cartesian coordinate system of $YFeO_3$ in a three-beam condition (3BC) with the $\mathbf{G}_{(022)}$ systematic reflections excited, where x along $\mathbf{G}_{(022)}$ is perpendicular to the (022) planes and y along [$\bar{1}\bar{5}5$] and the incident electron beam direction z along [15, 1, $\bar{1}$] are ~7° from [0$\bar{1}$1] and [100], respectively. (**b**-**d**) Beam-shift-dependent profiles of integrated RC_{emcd} for (**b**) $M_x(E)$, (**c**) $M_y(E)$ and (**d**) $M_z(E)$ calculated from the difference in integrated RC_{emcd} between the red and blue areas in q_y in the (**i**) schematic 3BC. (**e**-**g**) Beam shift-dependent profiles of integrated RC_{emcd} for (**e**) $M_x(E)$, (**f**) $M_y(E)$ and (**g**) $M_z(E)$ calculated from the integrated RC_{emcd} in the red area in q_y in the (**j**) schematic 3BC. The colored filled lines show contributions from each atomic plane, while the dashed lines represent the total signals. (**h**) Delocalization contributions of the Fe (022) planes labeled 1 through 6 to the target plane #5, showing the dominant contribution localized at plane #5 itself. (**i**–**j**) Schematics of the detector integration windows used for signal extraction: (**i**) Extraction strategy used for the profiles in (**b**–**d**), and (**j**) Extraction strategy used for the profiles in (**e**–**g**). (**k**) Quantitative comparison of the signal crosstalk, showing the relative contributions of the $M_x(E)$, $M_y(E)$, and $M_z(E)$ components for each extraction strategy. The data confirms the dominance of the target magnetic component in its respective optimized configuration.

https://doi.org/10.1038/s41565-026-02270-6



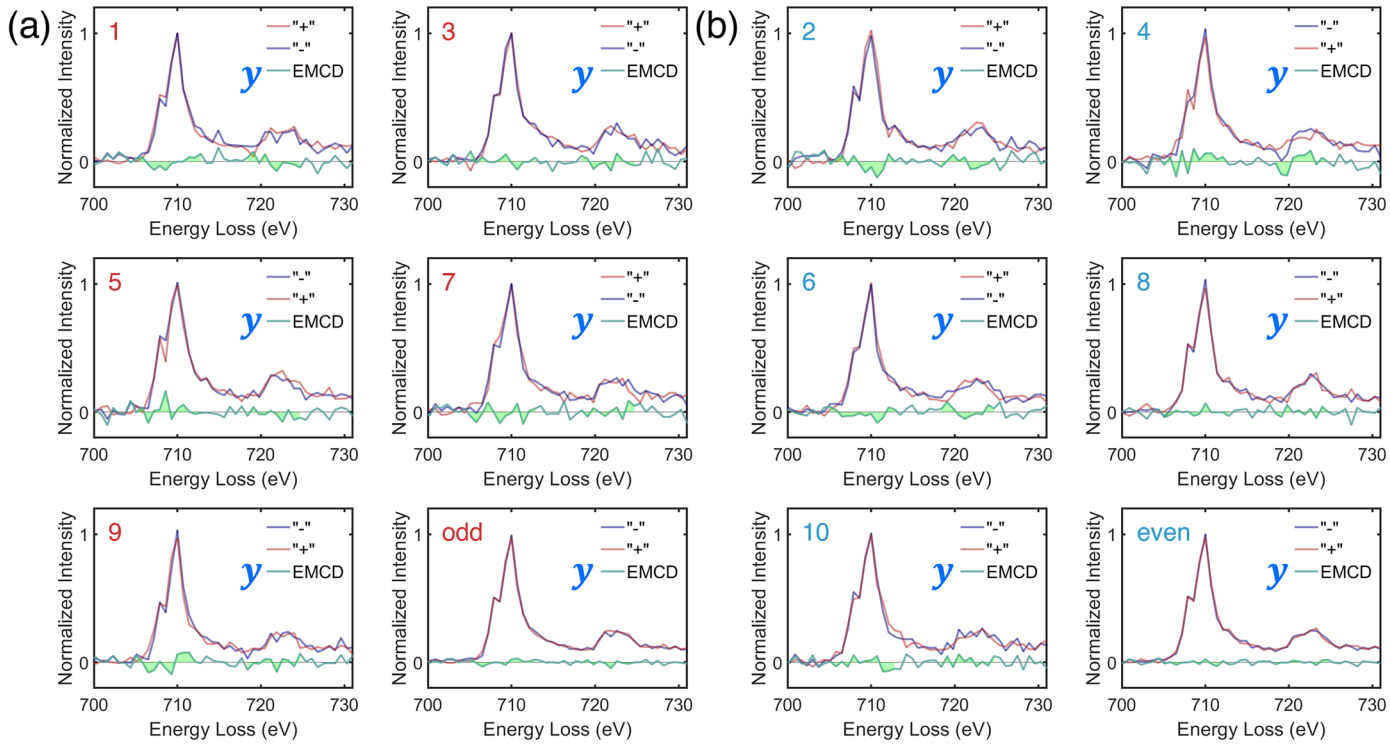
Extended Data Fig. 4 | Experimental and simulated ADF-STEM and EDS characterization under two three-beam conditions. Experimental and simulated annular dark-field (ADF) scanning transmission electron microscopy images and energy-dispersive X-ray spectroscopy (EDS) compositional color maps with Y in blue, Fe in green and O in red for $YFeO_3$ in three-beam conditions with (**a**) $\mathbf{G}_{(022)}$ and (**b**) $\mathbf{G}_{(202)}$ systematic reflections excited, together with corresponding line profiles (**c**) and (**d**), respectively and corresponding low-loss electron energy-loss spectra (**e**) and (**f**), respectively. All scale bars are 1 nm.

https://doi.org/10.1038/s41565-026-02270-6



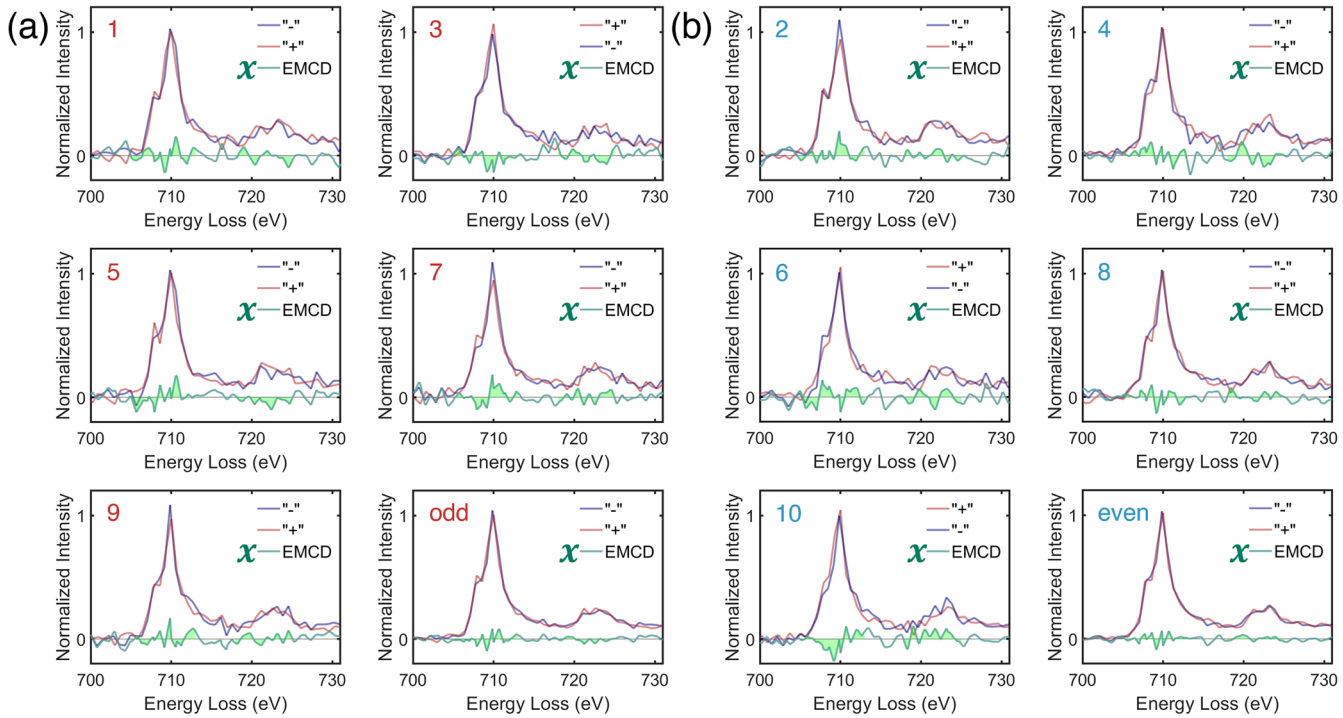
Extended Data Fig. 5 | Atomic-plane-resolved raw spectra obtained using the A_z analysis. Raw-data positive '+' electron energy-loss (EEL) spectra (red), negative '−' EEL spectra (blue) and electron magnetic circular dichroism (EMCD) spectra (green) for (**a**) each odd-numbered Fe (022) plane labeled 1 through 9 and their sum; (**b**) each even-numbered Fe (022) plane labeled 2 through 10 and their sum, extracted from a four-dimensional EMCD dataset for $YFeO_3$ in a three-beam condition with the $\mathbf{G}_{(022)}$ systematic reflections excited using the A_z analysis strategy, representing mainly the out-of-plane $M_z(E)$ component of the three-dimensional magnetization vector along the z axis as [15, $\bar{1}$,1].

https://doi.org/10.1038/s41565-026-02270-6



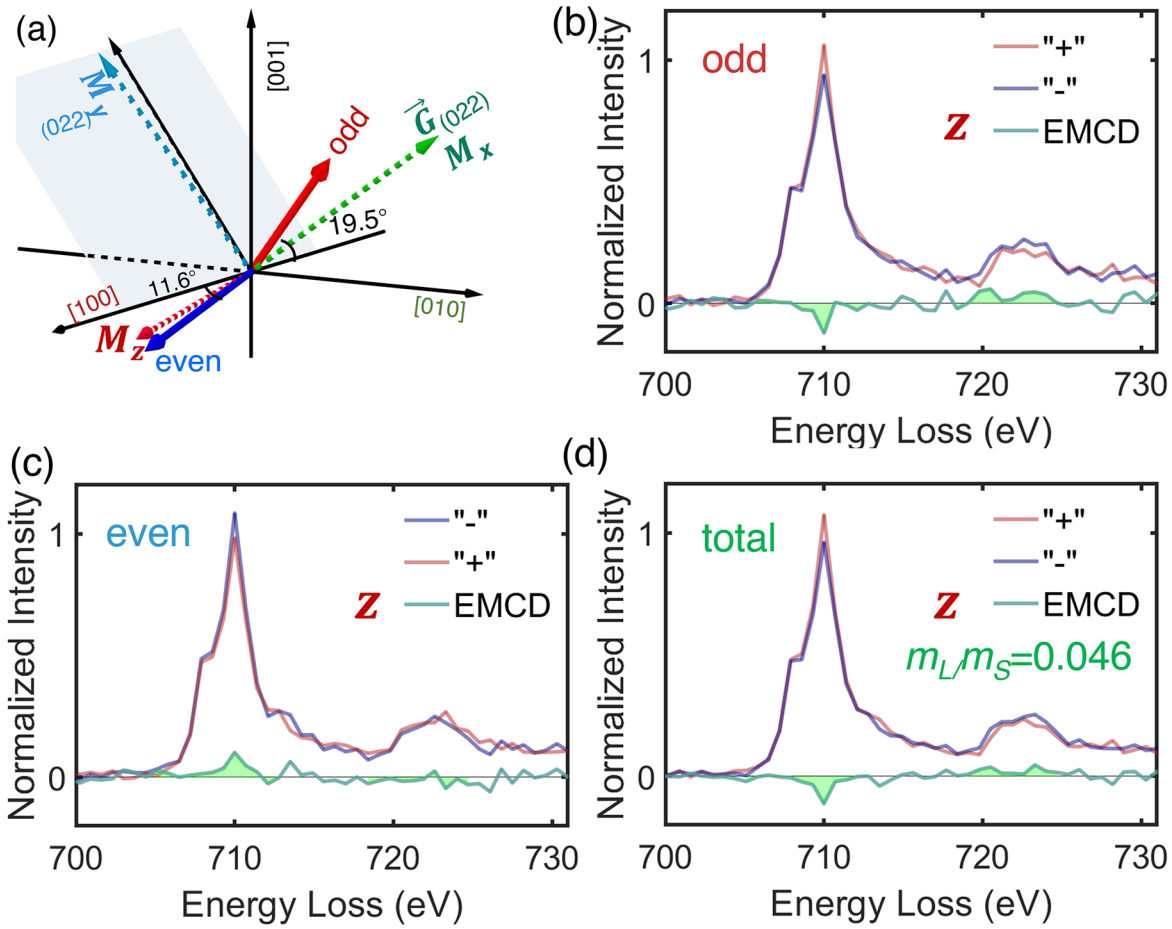
Extended Data Fig. 6 | Atomic-plane-resolved raw spectra obtained using the A_y analysis. Raw-data positive '+' electron energy-loss (EEL) spectra (red), negative '−' EEL spectra (blue) and electron magnetic circular dichroism (EMCD) spectra (green) for (**a**) each odd-numbered Fe (022) plane labeled 1 through 9 and their sum; (**b**) each even-numbered Fe (022) plane labeled 2 through 10 and their sum, extracted from a four-dimensional EMCD dataset for $YFeO_3$ in a three-beam condition with the $\mathbf{G}_{(022)}$ systematic reflections excited using the A_y analysis strategy, representing mainly the in-plane $M_y(E)$ component of the three-dimensional magnetization vectors along the y axis as $[\bar{1}\bar{5}5]$.

https://doi.org/10.1038/s41565-026-02270-6



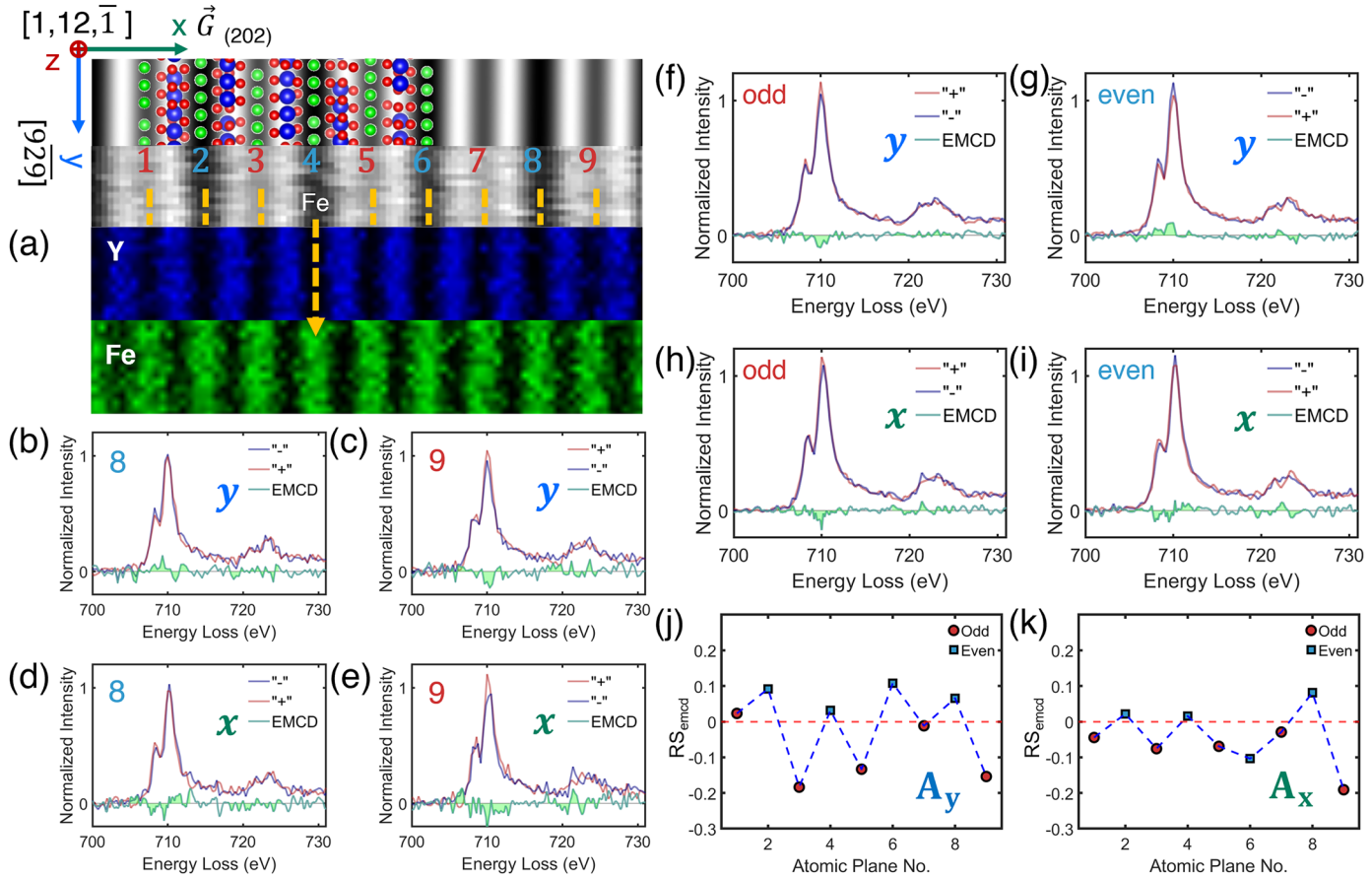
Extended Data Fig. 7 | Atomic-plane-resolved raw spectra obtained using the A_x analysis. Raw-data positive '+' electron energy-loss (EEL) spectra (red), negative '−' EEL spectra (blue) and electron magnetic circular dichroism (EMCD) spectra (green) for (**a**) each odd-numbered Fe (022) plane labeled 1 through 9 and their sum; (**b**) each even-numbered Fe (022) plane labeled 2 through 10 and their sum, extracted from a four-dimensional EMCD dataset for $YFeO_3$ in a three-beam condition with the $\mathbf{G}_{(022)}$ systematic reflections excited using the A_x analysis strategy, representing the in-plane $M_x(E)$ component of the three-dimensional magnetization vectors along the x axis as $\mathbf{G}_{(022)}$.

https://doi.org/10.1038/s41565-026-02270-6



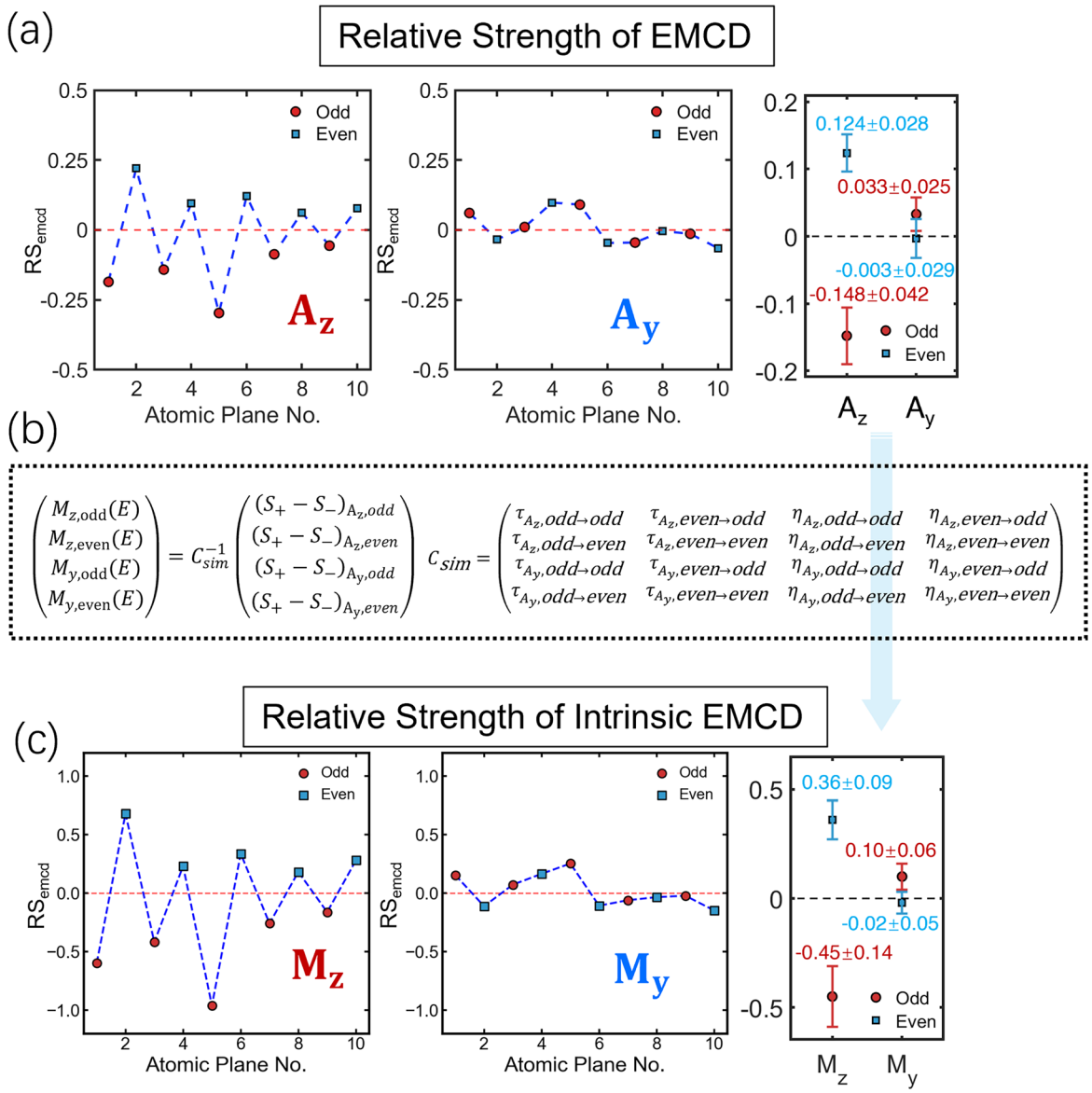
Extended Data Fig. 8 | Sublattice-resolved EMCD spectra and the orbital-to-spin magnetic-moment ratio. (**a**) 3D directions of magnetization vectors in the two antiferromagnetic spin sublattices with even-numbered and odd-numbered atomic planes, showing canting angles of 11.6° from [100] and 19.5° from [$\bar{1}$00], respectively. (**b, c**) Sum of Fe electron magnetic circular dichroism (EMCD), positive '+' and negative '−' electron energy-loss (EEL) spectra extracted from (**b**) all odd-numbered planes and (**c**) all even-numbered planes extracted from the four-dimensional EMCD dataset of $YFeO_3$ in a three-beam condition (3BC) with the $\mathbf{G}_{(022)}$ systematic reflections excited using the A_z analysis strategy and post-edge normalization. The EMCD spectra in (**b**) and (**c**) are almost identical to those in Fig. 4j and Fig. 4i, respectively, using $L_{2,3}$ edge normalization. (**d**) '+' EEL spectrum of the total planes, arising from the sum of the '+' EEL spectra of all odd-numbered planes and the '−' EEL spectra of all even-numbered planes; '−' EEL spectrum of the total planes, arising from the sum of the '−' EEL spectra of all odd-numbered planes and the '+' EEL spectra of all even-numbered planes. The EMCD spectrum of the total planes is achieved by subtracting the corresponding '+' EEL spectrum from the '−' EEL spectrum. The orbital-to-spin magnetic moment ratio (m_L/m_S) of the Fe atoms on the total atomic planes is calculated to be 0.046, demonstrating the almost quenched orbital magnetic moment.

https://doi.org/10.1038/s41565-026-02270-6



Extended Data Fig. 9 | Atomic-plane-resolved imaging of in-plane magnetization components in the complementary (202) geometry. Atomic-plane-resolved imaging of in-plane magnetization components in $YFeO_3$. (**a**) Atomic-resolution annular dark-field scanning transmission electron microscopy image and compositional map with Y in blue and Fe in green of $YFeO_3$ in a three-beam condition with the $\mathbf{G}_{(202)}$ systematic reflections excited in the second experimental Cartesian coordinate system with x along $\mathbf{G}_{(202)}$, y along $[9\bar{2}\bar{9}]$ and z along $[1,12,\bar{1}]$. The corresponding nine Fe (202) atomic planes are labeled 1 to 9. (**b**-**e**) Raw-data positive '+' electron energy-loss (EEL) spectra (red), negative '−' EEL spectra (blue) and EMCD spectra (green) from the two consecutive Fe (202) planes labeled (**b, d**) 8 and (**c, e**) 9 extracted from another four-dimensional (4D) electron magnetic circular dichroism (EMCD) dataset using the (**b, c**) A_y and (**d, e**) A_x analysis strategy, representing mainly the in-plane $M_y(E)$ and $M_x(E)$ components, respectively, of the 3D magnetization vectors. (**f**-**i**) The sum of the Fe EMCD, '+' and '−' EEL spectra extracted from (**f, h**) all odd-numbered (202) planes and (**g, i**) all even-numbered (202) planes using the (**f, g**) A_y and (**h, i**) A_x analysis strategy shows reversed EMCD signals between the odd-numbered and even-numbered (202) planes. The relative strengths of EMCD (RS_{emcd}) for the in-plane components extracted using the (**j**) A_y and (**k**) A_x analysis across the nine consecutive (202) planes shows almost-reversed signals between odd-numbered and even-numbered atomic planes, demonstrating antiferromagnetic coupling of Fe atoms on two adjacent (202) planes along in-plane x and y directions.

https://doi.org/10.1038/s41565-026-02270-6



Extended Data Fig. 10 | Simulation-assisted determination of intrinsic atomic-plane spin components. (**a**) Experimental relative EMCD strength (RS_{emcd}) profiles extracted using the A_z and A_y analysis across the ten consecutive atomic planes, together with statistical analysis results. (**b**) A system of linear equations describes the relationship between the intrinsic $M_z(E)$ and $M_y(E)$ components and the experimental EMCD spectra ($S_+ - S_-$) of each spin sublattice, where the C_{Sim} represents the matrix of dynamical diffraction simulation coefficients. (**c**) The corresponding simulation-assisted determination of relative strength of intrinsic EMCD for $M_z(E)$ and $M_y(E)$ components, after solving the system of linear equations. Summary symbols of (**a**) and (**c**) indicate arithmetic means and error bars represent the standard error of the mean (s.e.m.) across five odd-numbered planes (planes 1, 3, 5, 7 and 9; n = 5 spatial observations) or five even-numbered planes (planes 2, 4, 6, 8 and 10; n = 5 spatial observations) for each magnetic component.